Tracking Electromechanical Muscle Dynamics

R. Waasdorp

Master's Thesis

Neuromuscular Control Laboratory
in collaboration with
Acoustical Wavefield Imaging

Delft University of Technology

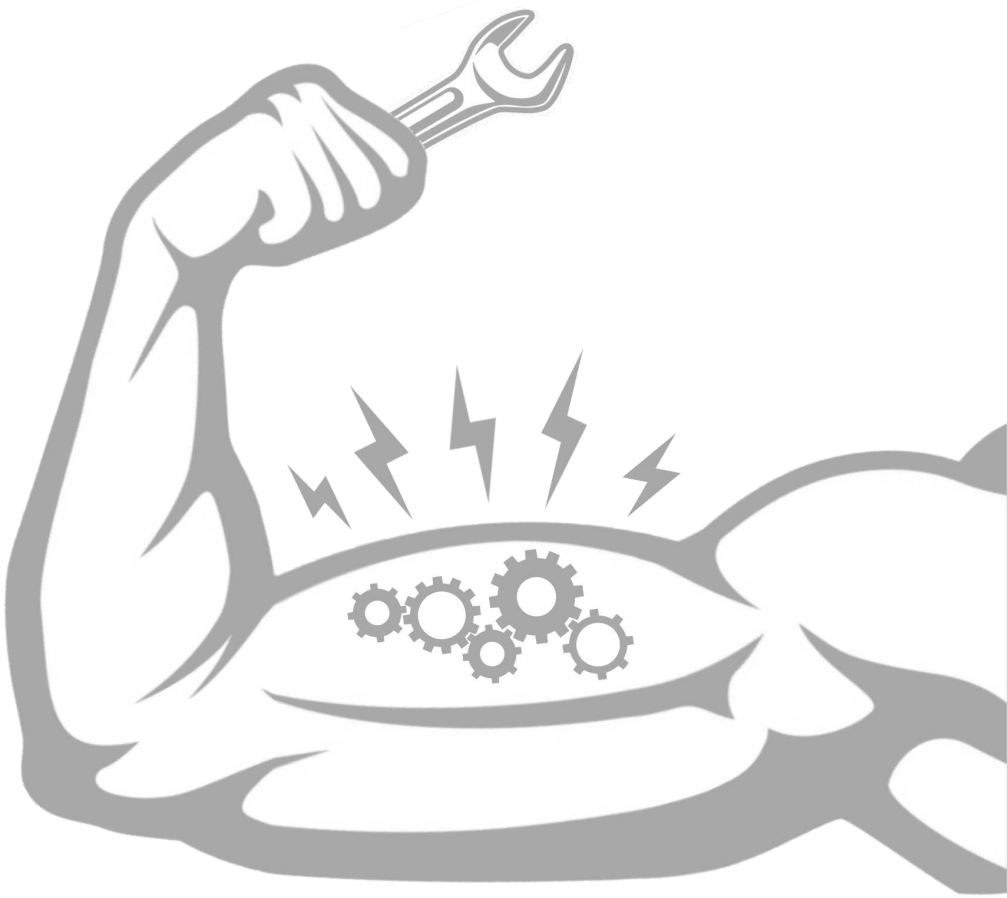

TU Delft

Tracking Electromechanical Muscle Dynamics

using ultrafast ultrasound and high-density EMG

by

R. Waasdorp

to obtain the degree of Master of Science
at the Delft University of Technology,
to be defended publicly on Wednesday December 11, 2019 at 11:00 AM.

Student number:	4295617	
Thesis committee:	Dr. Verya Daeichin	Acoustical Wavefield Imaging, TU Delft
	Dr. ir. Winfred Mugge	Neuromuscular Control Laboratory, TU Delft
	Dr. ir. Alfred Schouten	Neuromuscular Control Laboratory, TU Delft
	Dr. ir. Gerwin Smit	Biomechanical Engineering, TU Delft
	Prof. dr. ir. Nico de Jong	Acoustical Wavefield Imaging, TU Delft

This thesis is confidential and cannot be made public until December 11, 2021.

An electronic version of this thesis is available at `http://repository.tudelft.nl/`.

TU Delft ImPhys

Tracking electromechanical muscle dynamics using ultrafast ultrasound and high-density EMG

Rick Waasdorp, Winfred Mugge, Alfred C. Schouten, Verya Daeichin

***Abstract*—Muscles generate force and enable movement. After excitation of a muscle the muscle fibers contract. Methods to assess muscle contraction *in vivo* are scarce. Electromechanical delay (EMD), defined as the time lag between muscle excitation and contraction onset, has been proposed as a measure for contraction efficiency, but provides limited insight in electromechanical muscle dynamics. The current paper proposes and evaluates a novel non-invasive method to simultaneously track the propagation of both electrical and mechanical waves in muscles using high density electromyography and ultrafast ultrasound imaging (5 kHz). The method successfully tracked the propagation of the excitation-contraction (E-C) coupling in electrically evoked twitch contractions of the Biceps Brachii in three healthy participants. The excitation wave (i.e. action potential) had a velocity of 3.90 ± 0.65 m s^{-1} and the subsequent mechanical (i.e. contraction) wave had a velocity of 3.52 ± 0.89 m s^{-1}. Both waves propagated from distal to proximal and had similar spatiotemporal characteristics, indicating that our method can track the propagation of the E-C coupling. The experimental results were compared to simulated contractions of a newly developed multisegmental muscle fiber model, consisting of 500 sarcomeres in series. Both the experiment and simulation showed evidence that excited muscle sarcomeres pull on sarcomeres that were not yet reached by the action potential. In conclusion, our method can track the electromechanical muscle dynamics with high spatiotemporal resolution. Ultimately, the method can be used to characterize E-C coupling in patients with neuromuscular disease to assess contraction efficiency, monitor the progression of the disease and determine the efficacy of new treatment options.**

***Index Terms*—Ultrafast ultrasound, speckle-tracking, high-density electromyography, electrostimulation, wave tracking, skeletal muscle, muscle modeling, Hill, multisegmental modeling, excitation-contraction coupling, latency relaxation**

I. Introduction

Muscle contraction is a complex process, involving various electrochemical and electromechanical processes (for an extensive review, see Röhrle *et al.* 2019). A muscle contraction is initiated by a motor neuron, which generates an action potential (AP). The AP travels through a motor nerve which is attached to a muscle fiber at the neuromuscular junction (NMJ, also referred to as the motor end-plate). Upon arrival at the NMJ, the AP depolarizes a muscle fiber's cell membrane. The depolarization triggers a chain of cellular processes, which results in a wave like propagation of the AP along the muscle fiber in both directions towards the tendons. The velocity of an AP along a muscle fiber is typically in the range of 3–5 m s^{-1} (Moritani *et al.* 2004). As the excitation propagates longitudinally along the fiber, contraction onsets locally in a longitudinal fiber segment. A fiber segment consists of multiple myofibrils in parallel, and myofibrils consist of multiple sarcomeres in series. The sarcomeres are the smallest contractile units of a muscle, and upon depolarization of a fiber segment, cross bridges will start to form between actin and myosin filaments in a sarcomere. The cross-bridges allow generation of a contractile force by pulling the two filaments towards each other (Huxley, 1974). This sequence of reactions is referred to as the excitation-contraction (E-C) coupling (Sandow, 1952), and happens locally in the muscle fiber on a very fast timescale in the order of milliseconds. To clarify the terminology used throughout the paper, the term 'local' refers to a process happening in a segment of a fiber, which differs from considering the muscle as a whole.

The contractile force within a sarcomere is transmitted through various pathways to the tendons (Patel and Lieber, 1997). The exact way forces are transmitted is cause for debate, but a clear distinction can be made between force transmission in the intracellular structures and the extracellular matrix (ECM) (Yucesoy *et al.* 2002). Previous work indicated that various muscle pathologies affect the pathways of force transmission between these two domains, thereby affecting the muscle force generative capacity, i.e. contraction efficiency (Claflin and Brooks, 2008; Gillies and Lieber, 2011; Le *et al.* 2018).

Currently, there are no non-invasive techniques to assess muscle contraction efficiency and to track the E-C propagation. Non-invasive assessment of contraction efficiency is crucial in monitoring the progression of neuromuscular diseases, such as muscular dystrophies. In addition, assessment of contraction efficiency can be used to study the effect of training in sports engineering, and monitor the healing process of muscle injuries. Several studies proposed to assess the electromechanical delay (EMD) as a measure for contraction efficiency. The EMD is defined as the time lag between onset of muscle electrical activity and force production at whole muscle scale (Cavanagh and Komi, 1979). However, the EMD at whole muscle scale provides no insight in the local E-C and mechanisms of force transmission.

Nordez *et al.* (2009) proposed to combine measurement of the EMD with assessment of the time of muscle fiber motion onset and tendon motion onset using ultrafast ultrasound imaging (UUI) in electrostimulated twitch contractions. Assessment of the onset of fiber and tendon motion in addition to force production onset gives a more complete characterization of the electromechanical processes involved in muscle contraction (see overview in Fig. 1a). However, the obtained tissue velocities were averaged over a very large region of interest (ROI), more specific, the entire ultrasound field of view (FOV) of the muscle belly (Hug *et al.* 2015; Lacourpaille *et al.* 2017, 2013a,b; Nordez *et al.* 2009). By averaging over this

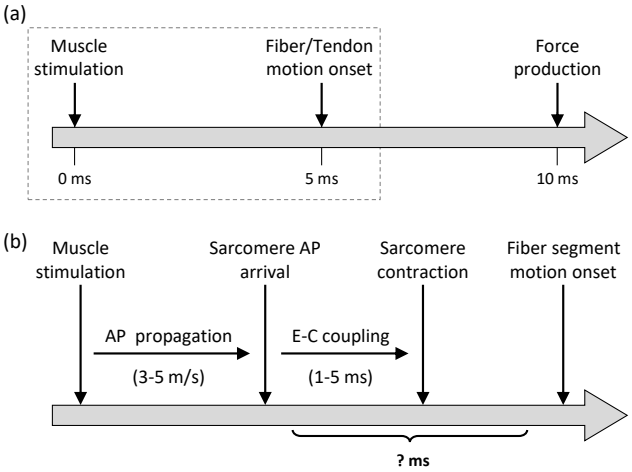

Fig. 1: (a) Schematic representation of time-line in the electromechanical delay (EMD). The classical EMD comprises the delay between stimulus and force production onset. Nordez *et al.* (2009) proposed a more complete characterization of the EMD by including motion onset of muscle fibers and the myotendinous junction (tendon-muscle fiber attachment point). Bicep motion onset and force onset timing adapted from Nordez *et al.* (2009). There are currently no methods to measure the local electromechanical processes within the gray dashed square, which are schematically represented in **(b)**. After a stimulus, an AP propagates along the fiber, causing the local fiber segments, i.e. sarcomeres, to be activated. Upon activation, cross-bridges will form within a sarcomere, causing the sarcomere to contract. This causes a local active motion onset in the fiber segment. E-C coupling timing adapted from Sandow (1952), based on single-fiber experiments. There is limited *in vivo* data available on the dynamics of the processes included in the brace under the arrow, indicated by the question mark.

large ROI, the E-C propagation cannot be tracked, hence the method gives limited insight in the electromechanical processes and contraction efficiency.

We propose a novel method that combines high-density surface electromyography (HD-sEMG) and UUI to follow the E-C propagation by simultaneously tracking of the propagating excitation wave (the AP), and the subsequent local motion caused by the contraction (i.e. a mechanical wave). In depth analysis of the local E-C coupling (depicted in Fig. 1b) can advance our understanding of muscular behavior, muscle force transmission and the pathophysiology of neuromuscular diseases.

The proposed method was evaluated in three healthy participants. To assess the validity of the experimental results, a novel nonlinear micromechanical muscle fiber model was developed. The model allowed simulation of the E-C propagation through a single muscle fiber on a millisecond time scale. In literature, a wide variety of computational muscle models can be found, however, the currently available muscle models are not directly applicable to study propagation of the E-C coupling. The majority of muscle models reduce the whole muscle to a single contractile element (Hill, 1953; Huxley, 1957). Consequently, the whole muscle has to be activated simultaneous, neglecting the E-C propagation. Studies that did model multiple contractile elements either considered a long (i.e. tens of milliseconds) time scale (Van Leeuwen and Kier, 1997; Yekutieli *et al.* 2005) or activate all contractile elements simultaneous (Campbell, 2009; Günther *et al.* 2012; Morgan *et al.* 1982; Stoecker *et al.* 2009), thereby limiting their use to study the E-C coupling.

The objectives of this paper are to (1) describe and evaluate a novel method to track the E-C propagation *in vivo* by combining UUI and HD-sEMG, and (2) validate the experimental results by simulating muscle contractions with the newly developed fiber model. We found that the experimental method can successfully track the excitation wave (AP) and subsequent mechanical wave with high spatio-temporal resolution. Both excitation and mechanical wave propagated from distal to proximal. Mean (SD) velocities for the AP and mechanical wave were found to be 3.90 (0.65) $\mathrm{m\,s^{-1}}$ and 3.52 (0.89) $\mathrm{m\,s^{-1}}$, respectively. The fiber model could reproduce the experimentally observed mechanical response to a propagating AP excitation. In conclusion, our method can track the fast muscular electromechanical dynamics with high spatio-temporal resolution by combining ultrafast ultrasound imaging and high-density electromyography. Ultimately, the method can be used to characterize the E-C coupling *in vivo* in patients with neuromuscular disease to assess contraction efficiency, monitor the progression of neuromuscular disease and determine the efficacy of new treatment options.

II. Methods

Three healthy male subjects (22-25 years) participated in the experiment. The participants gave informed consent. The experiment was approved by the TU-Delft ethics committee.

A. Instrumentation

1) Surface EMG activity

To track the action potentials, an 8×8 square high-density (HD) electrode grid (interelectrode distance $4\,\mathrm{mm}$) was placed proximal with respect to the innervation zone (IZ) over the belly of the Biceps Brachii (BB; see Fig. 2b and d). A reference Ag-AgCl electrode was placed on the wrist. Unipolar signals were sampled at $2048\,\mathrm{Hz}$ using a 136-channel Refa amplifier (TMSi, Oldenzaal, the Netherlands).

2) Electrical stimulation

Muscle contractions of the BB were evoked by electrical stimulation. The stimulator (Micromed Energy, Micromed S.p.A., Mogliano Veneto, Italy) gave a single pulse with only negative phase, with a pulse duration of $200\,\mu\mathrm{s}$ and an amplitude between 5-10 mA. The cathode was placed over the innervation zone of the BB, which is located on the distal part of the BB (Barbero *et al.* 2012).

3) Ultrasonography

Muscle contractions were imaged using a linear transducer array (L12-5 $50\,\mathrm{mm}$ 256 element probe; Philips, Bothell, WA, USA) connected to a Vantage-256 research ultrasound scanner (Verasonics Inc., Kirkland, WA, USA). The scanner was set to transmit plane waves with a center frequency of $7.8\,\mathrm{MHz}$, and sampled the raw radio frequency (RF) signals at 4 times the center frequency.

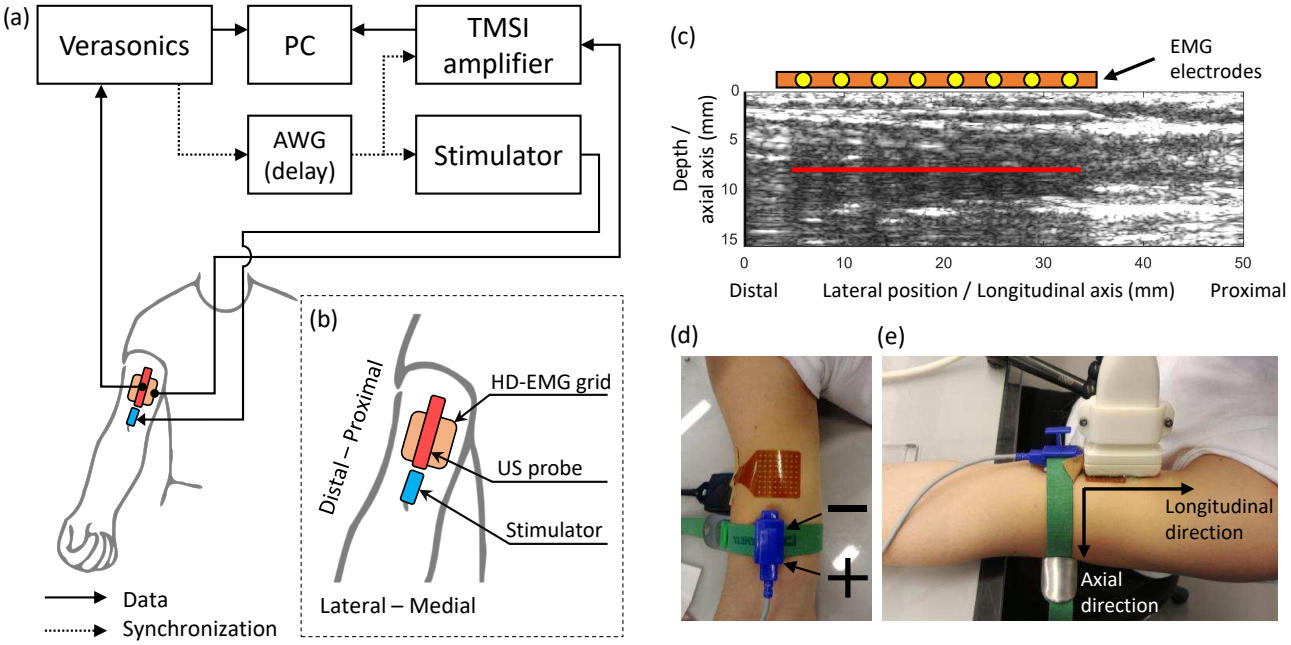

Fig. 2: Overview of the experimental setup. **(a)** Schematic of experimental setup showing the connections between the measurement equipment and stimulator. The solid black arrows represent data connections, the dashed lines represent TTL signal connections for synchronization of the equipment. The Verasonics ultrasound scanner sent a TTL trigger to the arbitrary waveform generator (AWG), the AWG was set to a delay of 20 ms after which it sent a trigger to the TMSI EMG amplifier and the muscle stimulator. **(b)** Zoom-in of the positioning of the measurement equipment on the Biceps Brachii (BB). The stimulator (blue rectangle) was positioned over the innervation zone, which is located on the distal part of the BB. The HD-EMG electrode grid (orange square) was placed proximal with respect to the stimulator and the ultrasound probe (red rectangle) was positioned over the center of the HD-EMG grid. **(c)** Ultrasound image of the Biceps Brachii (BB), the EMG electrodes are depicted on top of the ultrasound image. The red line denotes one of the M-modes that were used in the analysis. The acoustic shadow caused by the HD-EMG grid is visible directly beneath the HD-EMG grid. **(d)** Stimulator positioned on the innervation zone (IZ) of the BB, the cathode was placed on the proximal side. **(e)** Ultrasound transducer placed on top of the HD-EMG electrodes. The arrows denote the coordinate system.

Since the scanner consists of 128 channels per transducer connector, one image was formed with three synthetic aperture transmit and receive events. Imaging depth was set to 16 mm, resulting in an effective frame rate of 5000 frames per second. Per trial 500 frames were recorded, corresponding to 100 ms.

4) Triggering and synchronization

To trigger the stimulator and to allow synchronization of the recordings of the ultrasound scanner and EMG amplifier in data processing, a transistor-transistor logic (TTL) pulse was sent from the ultrasound scanner to an arbitrary waveform generator (AWG; DG1022A, Rigol, Beijing, China) at the start of each ultrasound acquisition. Upon receipt of the TTL pulse by the AWG, the AWG transmitted a TTL signal to the inputs of the EMG amplifier and stimulator after a delay of 20.00 ms. The delay allows the ultrasound scanner to start recording ultrasound frames prior to the contraction, to have sufficient baseline without motion (see overview in Fig. 2a).

B. Protocol

Participants were seated in a comfortable height-adjustable chair and were asked to rest their arm on the table. First, the IZ of the BB was detected by placing the stimulator on the distal portion of the BB, around ⅔ of the length of the BB. The stimulator was moved around over the BB while repeatedly stimulating, until a point with most intense contraction was found (determined visually). Once found, the stimulator was fixated using an elastic arm strap. Before placement of the EMG electrodes, the skin on the upper arm and wrist was shaved and cleaned with an abrasive skin preparation gel and alcohol to reduce skin impedance. Next, the ultrasound transducer was placed on top the HD-sEMG electrode grid, and fixated using a 6 degree-of-freedom mechanical magnetic measuring stand with central locking mechanism. The transducer position was adjusted such that the full HD-sEMG grid was in the FOV and the majority of the muscle fibers in the FOV were aligned with the longitudinal axis (verified by low frame rate real-time imaging).

The experiment consisted of three sets of ten electrical stimulations, with an inter-stimulus interval of 5 s and a 5 minute break between sets, totalling 30 contractions per participant. After the break, the stimulator position was checked to still elicit a contraction and adjusted if needed.

C. Processing

Ultrasound and EMG signals were processed in Matlab R2018b (The MathWorks, Natick, MA, USA).

1) EMG velocity estimation

EMG signals were first spatially filtered using the longitudinal single differential (longitudinal direction, Fig. 2c and e) to obtain bipolar signals (Stegeman *et al.* 2012).

Next, the signal was band-pass filtered using a bidirectional 3rd order Butterworth filter (cutoff frequencies 10-250 Hz). To find the velocity of the action potential propagating through the muscle, a custom fitting procedure was used. The bipolar EMG signals elicited by electrical stimulation typically have a negative and a positive peak with different amplitude and duration. Therefore, two sines with sufficient degrees of freedom to resemble the shape of the EMG signals were chosen as the basis for the fitting function. The measured bipolar signal per electrode over time is given by $y^m_{ij}(t)$, with $i = 1...N$ the electrode row (proximal to distal) and $j = 1...M$ the electrode column (medial to lateral). For the used 8×8 electrode grid, $N = 7$ and $M = 8$, corresponding to the 56 bipolar channels. The fitting function is given by,

$$\begin{aligned} y^s_{ij}(t) = w_{1ij}(t)\sin\left(\tfrac{2\pi}{T_1}\left(t-\tau_{ij}\right)\right) - \\ w_{2ij}(t)\sin\left(\tfrac{2\pi}{T_2}\left(t-\tfrac{T_1}{2}-\tau_{ij}\right)\right), \end{aligned} \tag{1}$$

with window functions,

$$w_{1ij}(t) = \begin{cases} A_1, & \tau_{ij} < t \le \tau_{ij} + \frac{T_1}{2} \\ 0, & \text{otherwise,} \end{cases} \tag{2a}$$

$$w_{2ij}(t) = \begin{cases} A_2, & \tau_{ij} + \frac{T_1}{2} < t \le \tau_{ij} + \frac{T_1+T_2}{2} \\ 0, & \text{otherwise.} \end{cases} \tag{2b}$$

The windows with different amplitudes and lengths allowed fitting on the asymmetric shaped action potentials. The delay τ_{ij} is given by,

$$\tau_{ij} = \tau_{\text{arr}} - \tau_{\text{x}ij} - \tau_{\text{y}ij}, \tag{3}$$

and depends on a common delay τ_{arr} depending on the distance of a reference electrode to the IZ, and a delay depending on the location of each individual electrode,

$$\tau_{\text{x}ij} = (i-1)\frac{d_{\text{ie}}}{V_{\text{ap}}}, \tag{4a}$$

$$\tau_{\text{y}ij} = (j-1)\frac{d_{\text{ie}}\tan(\theta)}{V_{\text{ap}}}, \tag{4b}$$

where d_{ie} denotes the interelectrode distance, V_{ap} the velocity of the action potential, and θ the angle of the propagating wave to accommodate for the skewness of end-plate positions on the muscle fibers (Stegeman *et al.* 2000).

For each participant and trial, the model was fit to normalized bipolar EMG data, i.e. $\bar{y}^m_{ij}(t) = y^m_{ij}(t)/\sigma_{ij}$, with σ_{ij} the standard deviation of channel ij. The parameter optimization was done in Matlab, using the `lsqnonlin` function. Channels with a root mean square (RMS) lower than $10\,\%$ of mean RMS of all channels were excluded from the fitting procedure. The fitting criterion was defined by,

$$E = \sum_{i=1}^{N}\sum_{j=1}^{M}\left\|\bar{y}^m_{ij}(t) - y^s_{ij}(t)\right\|^2. \tag{5}$$

The validity of the found parameters after convergence was assessed by the variance accounted for (VAF), which was determined per channel,

$$\text{VAF}_{ij} = \left[1 - \frac{\sum_{n_{ij}}^{m_{ij}}(\bar{y}^m_{ij}(t) - y^s_{ij}(t))^2}{\sum_{n_{ij}}^{m_{ij}}(\bar{y}^m_{ij}(t))^2}\right]\cdot 100\%, \tag{6}$$

where n_{ij} corresponds to the first and m_{ij} to the last sample within the window of channel ij, i.e. where $y^s_{ij}(t) \neq 0$. This was done to avoid influence of stimulation artifacts and complex MUAP shapes on the VAF that the model could not explain. Channels for which the fitting procedure resulted in a VAF lower than $20\,\%$ were excluded from the analysis. After exclusion of these channels, the parameter optimization was performed again. Next the mean VAF was determined as

$$\text{VAF} = \frac{1}{NM}\sum_{i=1}^{N}\sum_{j=1}^{M}\text{VAF}_{ij}. \tag{7}$$

The found parameters were used to simulate the EMG signal as a reference to find the onset of tissue motion, described below. The velocity of the AP was taken as the optimized parameter V_{ap}. The arrival time of the AP, $T_{\text{arr-ap}}$, was defined as the time instant of the depolarizing peak in the simulated EMG, at the most distal electrode beneath the US probe (depicted in Fig. 3b).

2) Ultrasonography

Raw RF signals were processed to In phase-Quadrature data using conventional delay and sum beamforming, resulting in $S(x, z, t_i)$. The EMG and ultrasound data were spatially aligned using the acoustic shadow present due to the electrode grid (see Fig. 2c). Tissue velocities $v_z(x, z, t_i)$ along the ultrasound beam axis (i.e. z-axis, depth Fig. 2c) were determined using one-lag autocorrelation speckle tracking (Deffieux *et al.* 2008). Since only axial velocities are determined, the obtained velocities do not directly reflect muscle fiber elongation, but rather muscle fiber thickening and thinning. The tissue velocities v_z were temporal filtered using a bidirectional 3rd order Butterworth low-pass filter (cutoff frequency $100\,\text{Hz}$). Next v_z was differentiated to obtain axial tissue acceleration a_z,

$$a_z(x, z, t_i) = \left(v_z(x, z, t_i) - v_z(x, z, t_{i-1})\right)F_s, \tag{8}$$

with F_s the frame rate. The mechanical wave was tracked using a normalized Radon transform of the acceleration a_z (Vos *et al.* 2017). To find the onset of tissue motion, only $a_z(x, z, t_i)$ within a time window of moment of first detection of EMG activity and the second (positive) peak in the EMG was used,

$$\min_{ij}(\tau_{ij}) - 5\,\text{ms} < t_i \le \min_{ij}(\tau_{ij}) + \tfrac{T_1}{2} + \tfrac{T_2}{4}. \tag{9}$$

Furthermore, only data in a region of interest (ROI), chosen directly below the EMG grid, was used to track the mechanical wave (horizontal lines in Fig. 4). Three different horizontal M-modes in the ultrasound image with good speckle from the muscle fibers were chosen for the analysis. Acceleration data along these M-modes (averaged over $\pm 0.5\,\text{mm}$ in depth), within the ROI and the time of window of interest was used to track the mechanical wave, resulting in a velocity V_{conw} and time of arrival $T_{\text{arr-conw}}$. Peaks in the Radon transform corresponding to a velocity outside $V_{\text{ap}} \pm 2\,\text{m}\,\text{s}^{-1}$ were regarded as false positives and excluded.

D. Fiber model

Various studies have modelled muscle as a multisegmental system comprising multiple Hill models in series, however all assumed instantaneous muscle activation (Günther *et al.* 2012; Morgan *et al.* 1982; Stoecker *et al.* 2009). Other studies that modelled whole muscle as a series of Hill models considered a time scale of seconds, limiting their use to study the E-C dynamics (Van Leeuwen and Kier, 1997; Yekutieli *et al.* 2005). Therefore, a multisegmental fiber model conceptually similar to the model by Morgan *et al.* (1982) was implemented. By sequentially activating the individual sarcomeres, the fiber response during the first milliseconds of muscle contraction was simulated. The full model description can be found in Appendix B.

1) Fiber mechanical properties

The muscle fiber was modelled as a large chain of $n = 500$ sarcomeres in series. In the following, the subscript i denotes sarcomere number. The force in sarcomere i is described by the Hill model, relating the sarcomere length $\ell_i(t)$, velocity $\dot{\ell}_i(t)$ and activation $a_i(t)$ to force $F_{\mathrm{s},i}(t)$. Only the parallel and contractile elements were considered for an individual sarcomere, separating the force in an active part due to cross-bridge interactions, and a passive part caused by connective tissue in the fiber. Hence the force per sarcomere is given by,

$$F_{\mathrm{s},i}(t, \ell_i, \dot{\ell}_i) = F_{\mathrm{PE},i}(\ell_i) + f_{\mathrm{a},i}(t) F_{\mathrm{CE},i}(\ell_i, \dot{\ell}_i), \qquad (10)$$

where F_{PE} denotes the passive sarcomere force, F_{CE} the active sarcomere force and f_{a} the sarcomere activation function. The sarcomeres are separated by boundaries, i.e. Z-disks, which are represented by a 1D array of $m = n+1$ point masses (i.e. nodes), where boundary j has position $x_j(t)$. The first boundary is fixed, and the last boundary $x_m(t)$ is connected to a tendon, modelled as a linear spring. The tendon corresponds to the series element in the Hill model. The position of the other end of the tendon is given by x_t, and is fixed during muscle contraction.

To model the propagation of the action potential, the sarcomere activation $a_i(t)$ is dependent on the initial sarcomere position and the velocity of the action potential V_{ap}. The sequential activation of the sarcomeres is modelled by a linear increasing activation function $f_{\mathrm{a},i}$. The Hill model uses an input signal in the interval $[0, 1]$, where $f_{\mathrm{a},i} = 0$ corresponds to an inactive sarcomere and $f_{\mathrm{a},i} = 1$ to a fully activated sarcomere. The activation function of sarcomere i is given by a linear increasing ramp function,

$$f_{\mathrm{a},i}(t) = \begin{cases} 0, & t \le t_{\mathrm{d},i}, \\ \dfrac{t - t_{\mathrm{d},i}}{t_{\mathrm{a},i}}, & t_{\mathrm{d},i} < t \le t_{\mathrm{d},i} + t_{\mathrm{a},i}, \\ 1, & t > t_{\mathrm{d},i} + t_{\mathrm{a},i}, \end{cases} \qquad (11)$$

with $t_{\mathrm{d},i}$ the delay for activation onset and $t_{\mathrm{a},i}$ the time required to reach full activation. The delay for activation onset $t_{\mathrm{d},i}$ for sarcomere i due to propagation time for the action potential along the fiber is given by,

$$t_{\mathrm{d},i} = \frac{\sum_{k=1}^{i-1} (\ell_{\mathrm{optim,k}}) + \frac{1}{2}\ell_{\mathrm{optim,i}}}{V_{\mathrm{ap}}} + t_{\mathrm{ss}} \qquad (12)$$

with $\ell_{\mathrm{optim},i}$ the optimum length of the sarcomere, t_{ss} a general delay term and V_{ap} the velocity of the action potential.

A damping force was implemented on the nodes between the sarcomeres, to avoid expected high frequency oscillations due to the low mass of the fiber. The damping force on node $x_j(t)$ is given by,

$$F_{\mathrm{damp},j}(t) = -c_{\mathrm{damp},j}\ \dot{x}_j(t), \qquad (13)$$

with $c_{\mathrm{damp},j}$ the damping coefficient for node j. Since the distal boundaries (close to the tendon) are expected to have higher velocities than the proximal boundaries, the damping coefficient for boundary j is scaled by its initial position $x_{0,j}$,

$$c_{\mathrm{damp},j} = \begin{cases} c_{\mathrm{damp}}, & j = 0, \\ \frac{c_{\mathrm{damp}}}{x_{0,j}}, & j > 0. \end{cases} \qquad (14)$$

This scaling of the damping can be justified by considering that during a whole muscle contraction the intramuscular fluid will move together with the rest of the muscle structure. Hence the fluid will have a lower relative velocity with respect to the Z-disks then in the modelled fiber, where the surroundings are fixed.

To study the effect of damping and velocity of the action potential, six different fiber designs with different parameters were simulated (see Table 1). The velocity of the action potential V_{ap} was either slow, fast or infinity (where infinity corresponds to simultaneous activation of all sarcomeres). The nodal damping was either strong or weak. The other model parameters were kept constant (see Table B1).

Table 1: Different muscle fibers and the parameters used. Other parameters were kept constant (see Table B1). Abbreviation for each design for short reference, first letter V denotes velocity of action potential V_{ap} (either `S` slow, `F` fast or `I` instant), second letter C denotes damping on nodes c_{damp} (either `S` strong or `W` weak).

Abbreviation	V_{ap} ($\mathrm{m\,s^{-1}}$)	Node damping ($\mu\mathrm{N\,s\,m^{-1}}$)
$\mathtt{V_S C_W}$	1	10
$\mathtt{V_S C_S}$	1	100
$\mathtt{V_F C_W}$	5	10
$\mathtt{V_F C_S}$	5	100
$\mathtt{V_I C_W}$	instant (∞)	10
$\mathtt{V_I C_S}$	instant (∞)	100

2) Simulation procedure

Numerical integration of the fiber model was done using Matlab 2018b (The MathWorks, Natick, MA, USA). Since the system has very low mass, the stiff `ode15s` solver was used for numerical integration. Tolerances were set to 1×10^{-10} and integration time was set to $20\,\mathrm{ms}$. Since ODE solvers cannot handle discontinuous functions well, continuous functions were fit to the piecewise continuous functions from the Hill model (described in Appendix B).

The initial condition for the fiber was set to zero velocity and an initial strain ε_0 of $7.5\,\%$, causing passive pre-tension in the fiber, as was the case in the experiment. The fiber consisted of 500 sarcomeres in series to have a sufficiently long fiber causing sufficient time between onset of activation between distal and proximal sarcomeres.

3) Model validation

No attempt to fit the model on experimental data was made. The large number of parameters and degrees of freedom in the model were expected to cause a problem for parameter optimization. Furthermore, the parameters obtained in such optimization do no directly reflect the underlying physiology since the Hill model is a phenomenological model. Therefore, an alternative way to validate the behavior of the model is proposed, by using the output of the multisegmental Hill (mH) model as input to a single segment Hill model (sH). The sH model has no propagating activation signal and therefore it can be expected that mH and sH predict different force output during contraction onset. However, if the mH model converges to the same force produced after the initial transient this validates the mH model, since the sH model has been validated extensively in literature.

From the length and velocity of the mH model, the strain and strain rate of the whole fiber was determined using the fiber optimum length (i.e. the sum of the optimum length of all sarcomeres of the mH model). This strain and strain rate was provided as input to the sH model. The activation per time step of the sH was chosen as the mean activation over all sarcomeres of the mH model,

$$a_{\mathrm{sH}}(t) = \frac{1}{N}\sum_{i=1}^{N} a_i(t). \tag{15}$$

If the ratio between the force in the sH and mH model (mH/sH) approached 1 at the final simulation time, this validates the mH model.

4) Comparison fiber designs

To quantitatively compare the different fiber designs listed in Table 1, various metrics were used. To see whether there are non-uniformities at different locations in the fiber, the mean sarcomere length and velocity was determined for a proximal and a distal section. The proximal section (i.e. first activated) was given by taking the mean over sarcomeres 100 to 200. The distal section was taken as sarcomeres 300 till 400. The electromechanical delay (EMD) was determined as the time at which the force reached $10\,\%$ of maximum isometric force. The power of the force of sarcomere i was determined by,

$$P_i(t) = \dot{\ell}_i(t) F_{\mathrm{s},i}(t, \ell_i, \dot{\ell}_i, a_i). \tag{16}$$

Furthermore, the work done by each sarcomere was determined. The work done by the force in sarcomere i at time instant t is given by,

$$W_i(t) = F_{\mathrm{s},i}(t)\Delta\ell_i(t) = F_{\mathrm{s},i}(t)\left(\ell_i(t+\Delta t) - \ell_i(t)\right). \tag{17}$$

Note that $W_i(t)$ is not affected by the damping on the nodes. To assess the contraction efficiency of the different

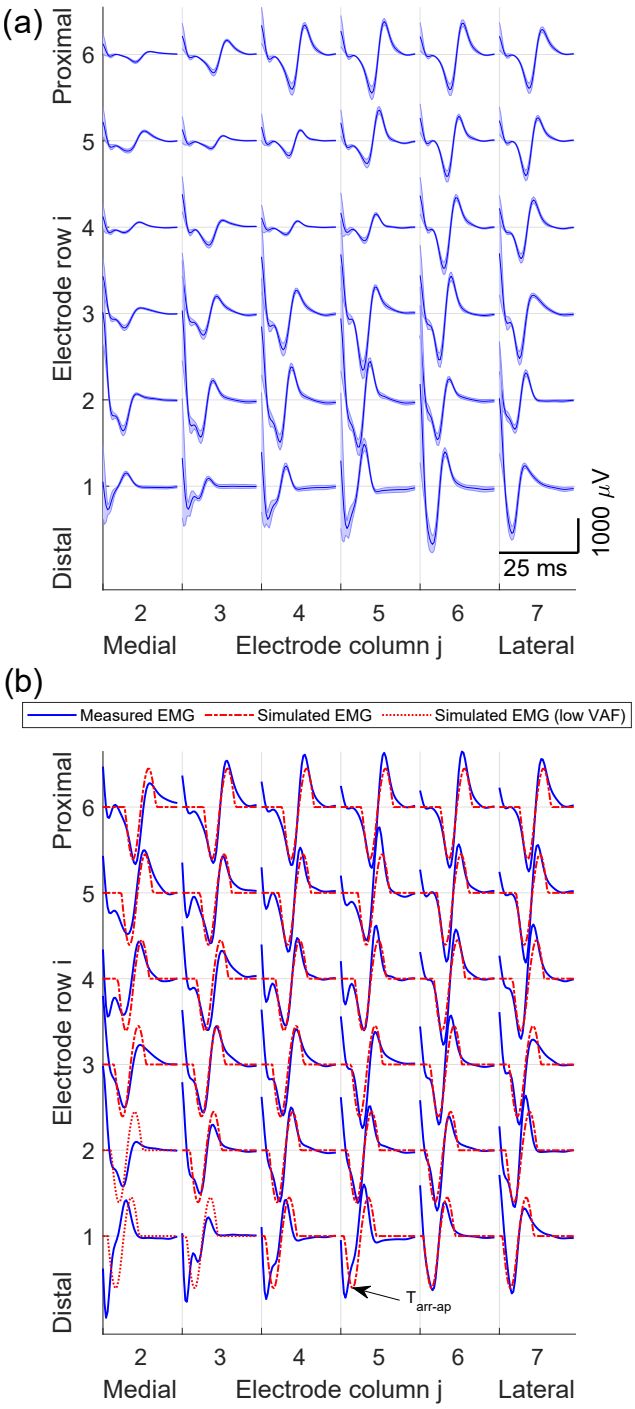

Fig. 3: Experimental result, EMG repeatability and fitting procedure. The most proximal bipolar EMG signal row and the most medial and lateral columns are omitted for readability (i.e. row 8 and column 1 and 8). All traces are 25 ms long, and start at the moment of stimulation. **(a)** Measured EMG signals of all electrodes y_{ij}^m for one set, blue thick line denotes mean of 10 stimuli, blue area denotes standard deviation. The low standard deviation indicates that there was a high repeatability across trials within a set. At the start of each signal, the stimulation artifact can be seen. **(b)** Typical result of the fitting procedure, shown data is of participant 1, blue lines denote the recorded bipolar EMG signals (normalized), $\bar{y}_{ij}^m(t)$. The red dashed lines denote the simulated output of the fitting procedure with optimized parameters, $y_{ij}^s(t)$. The channels for which the parameter optimization resulted in a VAF lower than 20% are plotted with dotted red lines (bottom left). The time of arrival for the AP, $T_{\text{arr-ap}}$, is indicated by the black arrow. The electrode column over which the ultrasound probe was positioned was chosen to determine $T_{\text{arr-ap}}$, in this example column 5. For this data set, the parameter optimization resulted in $V_{\text{ap}} = 3.67\ \mathrm{m\,s^{-1}}$ and the AP time of arrival was found to be $T_{\text{arr-ap}} = 5.37$ ms.

Table 2: Experimental results for three participants, M denotes mean, SD standard deviation, SR success rate. The velocity of the action potential V_{ap} was found for all trials (SR EMG fit). $T_{\text{arr-ap}}$ denotes the arrival time of the depolarizing peak in the action potential. The number of successful fits and the results for Radon transforming acceleration data to find the velocity V_{conw} of the contractile wave are presented for three M-modes at various depths. $T_{\text{arr-conw}}$ denotes the arrival time of the contractile wave.

Participant	SR EMG fit	V_{ap} (m s^{-1}) M	SD	$T_{\text{arr-ap}}$ (ms) M	SD	VAF (%) M	SD	M-mode depth (mm)	SR Radon fit	V_{conw} (m s^{-1}) M	SD	$T_{\text{arr-conw}}$ (ms) M	SD
1	30/30	3.71	0.082	6.48	1.96	81.47	3.49	5	26/30	3.48	1.30	7.20	4.77
								10	15/30	4.14	0.78	0.56	0.81
								14	20/30	4.04	0.82	1.75	2.00
2	30/30	4.73	0.349	9.38	0.81	77.58	7.85	5	20/30	2.89	0.34	11.12	1.24
								12	18/30	4.01	1.14	7.02	3.23
								14	28/30	3.18	0.27	8.84	0.83
3	30/30	3.27	0.086	10.87	0.42	77.29	2.56	5	29/30	3.34	0.38	14.97	0.72
								10	15/30	3.26	1.11	9.87	2.86
								14	9/30	3.84	0.36	10.94	0.66

fiber designs, the negative work done by the sarcomeres was determined. The total negative work in the fiber was determined by the sum of the work per sarcomere, for the time instants at which the sarcomere forces were in opposite direction of the sarcomere velocities. Finally, the dissipation due to nodal damping in the system was determined.

III. Results

A. Experimental results

Transcutaneous electrostimulation of the motor point of the Biceps Brachii successfully evoked muscle contractions in all participants, verified by the EMG recordings. All measured APs propagated from distal to proximal. The fitting procedure successfully estimated the velocity of the AP, V_{ap}, in all trials for all participants, see Table 2. The EMG measurement was highly repeatable, illustrated in Fig. 3a. A typical result for the fit on normalized EMG data is shown in Fig. 3b. The VAF of the fitting procedure was in 83 out of 90 trials above 70%, denoting reliable fits. The time of arrival of the depolarizing peak in the EMG, $T_{\text{arr-ap}}$, was in all trials well after the time instant of stimulus.

Propagating mechanical waves were observed in the tissue velocity profiles, as well as in the tissue acceleration profiles (see Fig. 4, 5 and Fig. A3). The Radon transform of the acceleration data within the ROI successfully tracked the mechanical waves in 83/90 trials. All waves propagated from distal to proximal. The tracking results varied with M-mode depth, and the total of 90 Radon transforms per participant resulted in a success rate of 57% for participant 1, 73% for participant 2 and 59% for participant 3 (see Table 2). Both the velocity, V_{conw} and time of arrival, $T_{\text{arr-conw}}$, of the mechanical wave had larger spread than the AP velocity and time of arrival, as can be seen by the standard deviations. In some cases, the arrival time of the mechanical wave preceded the arrival of the AP (e.g. participant 1, M-modes 10 and 14 mm, see Fig. A2). In most trials, the velocity and acceleration profiles showed a small positive peak first, which was followed by a negative peak (depicted in Fig. A3 and 5). The peaks in the acceleration profiles where more distinct than the peaks in the velocity profiles.

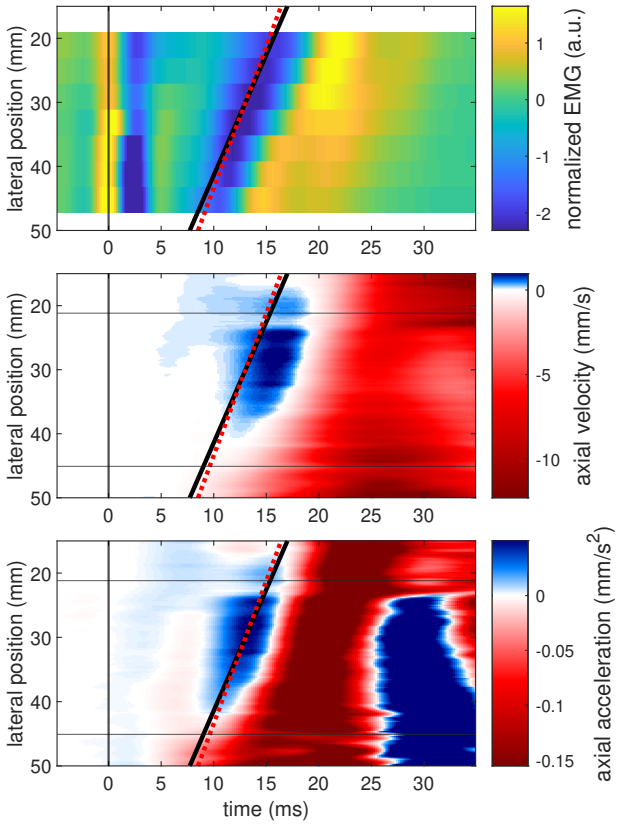

Fig. 4: Typical example of experimental results for participant 2, M-mode at depth 12 mm. Spatio-temporal representation of the EMG and ultrasound data. The horizontal axis represents time, with $t = 0$ the moment of stimulus. The vertical axis denotes lateral (i.e. longitudinal) position. AP propagated from distal to proximal, in this figure distal corresponds to lateral position approx. 50 mm, and proximal corresponds to approx. 20 mm. **(Top)** EMG signals of electrodes of the column directly beneath ultrasound probe. The fitting procedure resulted in a velocity of the action potential $V_{\text{ap}} = 4.43\,\text{m s}^{-1}$. The red dotted line denotes the depolarizing peak in EMG activity corresponding to $T_{\text{arr-ap}} = 9.60$ ms. The yellow peak at $t = 0$ ms is a stimulation artifact. **(Center)** axial tissue velocity along the M-mode. **(Bottom)** axial tissue acceleration. The acceleration data within the ROI was Radon transformed to track the contractile wave, resulting in velocity $V_{\text{conw}} = 3.77\,\text{m s}^{-1}$ and arrival time $T_{\text{arr-conw}} = 9.02$ ms. The tracked contractile wave is indicated by the black line in all three panels. Notice the asymmetric colorbars for the axial tissue velocity and tissue acceleration, causing the presumed precontractile motion to be depicted more clearly.

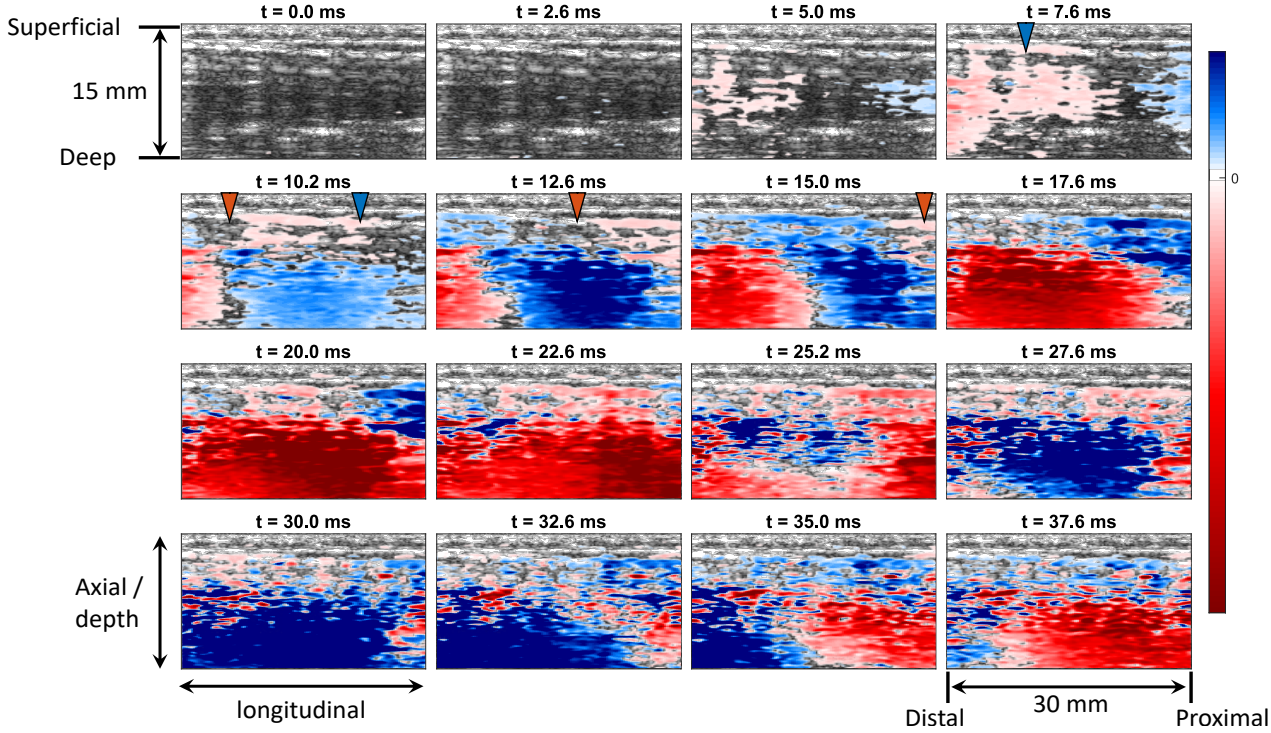

Fig. 5: Typical experimental result of axial tissue acceleration over time for participant 2. Blue denotes positive and red negative acceleration in axial direction, i.e. upward and downward motion respectively. The blue triangle at the top of a panel denotes the onset of EMG activity. The AP is propagating from left to right, i.e. distal to proximal. The orange triangle denotes the depolarizing peak in EMG activity. From 10 ms a positive acceleration wave propagates from left to right, likely caused by precontractile motion. The blue area is immediately followed by a red area, denoting higher amplitude negative acceleration, likely caused by the onset of muscle contraction. Around 24 ms the acceleration flips sign again, and a positive acceleration wave propagates from distal to proximal. Notice the asymmetric colorbar, to make the positive acceleration stand out more, showing the precontractile response more clearly.

Table 3: Quantitative comparison of simulation results for the different fiber designs. The parameters for the fiber design abbreviations can be found in Table 1. The column Ratio in force mH/sH shows the ratio at the end of the simulation, i.e. at $t = 20$ ms. The electromechanical delay (EMD) was determined as the time at which the force in the fiber reached 10% of maximum isometric force. The column Time max Power shows the time instant at which a fiber design reached maximum power output. The column Negative Work Total depicts the total negative work done by the sarcomeres, i.e. by both the passive and active sarcomere forces. Likewise, the column Negative Work Passive shows the negative work done by the passive forces in the sarcomeres. The last column, dissipation damping, shows the amount of energy dissipated in the system due to the nodal damping.

	Ratio force mH/sH	EMD (ms)	Time max Power (ms)	Max Power (μW)	Mean Power (μW)	Negative Work Total (nJ)	Negative Work Passive (nJ)	Work total (nJ)	Dissipation Damping (nJ)
$V_S C_W$	1.0225	0.72	1.46	5.43	0.459	701.0	438.0	9150	1380
$V_F C_W$	1.0225	0.32	1.09	8.05	0.449	36.5	36.5	8560	796
$V_I C_W$	1.0225	0.19	0.99	8.14	0.443	0	0	8380	607
$V_S C_S$	1.0223	1.12	1.95	4.93	0.447	148.0	148.0	11700	3970
$V_F C_S$	1.0218	0.49	1.17	4.50	0.438	7.40	7.40	10400	2640
$V_I C_S$	1.0216	0.32	0.99	4.28	0.436	0	0	10200	2470

B. Fiber model results

The fiber model was able to simulate the propagation of the action potential, and the subsequent contraction onset of individual sarcomeres. Fig. 6 shows the whole fiber length, velocity and force for the first 4 ms. The behavior of the various fiber designs is different in the first couple of milliseconds of contraction, but converges to the same length, velocity and force after longer simulation time. When comparing only fibers with the same damping parameter, the order in which the fibers converge (i.e. reach minimum length) was instant activation (V_I), fast AP (V_F) and lastly slow AP (V_S). The convergence order was not affected by the damping. The same order was observed in the electromechanical delay (EMD) and time to reach maximum power output (see Table 3).

When looking at what happens locally in the muscle fiber, we see that there is non-uniformity in sarcomere length and velocity (see Fig. 7 and A4). The standard deviation in sarcomere length was larger in the distal portion of the fiber. Similarly, there was spread in sarcomere velocities, which was found to be larger in the strongly damped fiber designs. The standard deviation in sarcomere velocities was also larger in the fibers that simulated a propagating AP, as indicated by the area in Fig. 7.

Looking at the sarcomere lengths in Fig. 7 for the fibers that simulate the propagating AP, it can be seen that the sarcomeres are first elongated, and later start to shorten when the sarcomeres are locally activated. This effect is

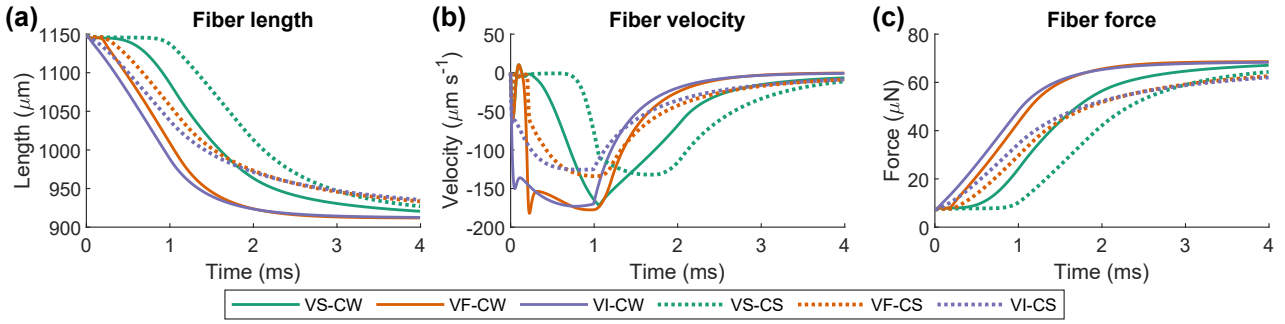

Fig. 6: Model simulation results of the onset of contraction for different fiber designs. The green lines represent the fibers with slow AP (V_S), the orange lines represent the fast AP (V_F), and the purple lines represent the instantaneous activated fibers (V_I). The solid lines represent the weakly damped fibers (C_W), and the dashed lines represent the strongly damped fibers (C_S). Full description of abbreviations in Table 1. **(a)** Whole fiber length during the first milliseconds of contraction. The whole fiber length for all fiber designs converged to the same length. The initial strain in the fiber was 7.5% with respect to optimum length, and the final whole fiber strain was –14.6%. **(b)** Whole fiber velocity during the onset of contraction. During the first milliseconds the velocities of the different fiber designs vary a lot. The velocities converge to zero after the initial transient. **(c)** Force in the fiber, determined by the state of the tendon. As expected, the force converges approximately to the maximum isometric sarcomere force.

clearly visible in the fiber with slow AP, but also present in the fiber with fast AP (as can be seen in the sarcomere velocity traces). Furthermore, this effect is strongest in the distal portion of the fiber.

The negative work done was the highest in the fibers with slow action potential (see Table 3), independent of the damping parameter. There was no negative work done by the instantaneous activated fiber. The energy dissipation was highest in the strongly damped fibers. When looking at the total energy delivered for contraction per fiber design (i.e. subtracting the energy dissipated from the total work done by the sarcomere forces), the fibers all delivered similar amounts of energy (mean $\pm$ SD, 7755 ± 20 nJ).

IV. Discussion

A. Experimental results

The current study demonstrated that by simultaneously using high-density surface electromyography (HD-sEMG) and ultrafast ultrasound imaging (UUI), fast electromechanical muscle dynamics can be tracked. Propagating action potentials (AP) were detected in all trials. AP velocities were found to be within physiological range, as reported in literature (Farina *et al.* 2004; Röhrle *et al.* 2019). The highly repeatable EMG recordings were comparable to other studies that used transcutaneous muscle stimulation (Farina *et al.* 2004; Hu *et al.* 2016; Lindkvist *et al.* 2018; Merletti *et al.* 1998). The stimulation was done on the motor point with low current (< 10mA), and consequently, only superficial muscle fibers were stimulated. This was visually verified, as only very small movements of the skin were observed. Similar results of superficial stimulation were reported by Deffieux *et al.* (2008, see ref. Fig. 5 and 13).

The tracked mechanical waves had a velocity in the same order of magnitude as the AP velocity. The mean and standard deviation of the mechanical wave velocities were similar to values reported in previous studies (Deffieux *et al.* 2008; Deffieux *et al.* 2006; Grönlund *et al.* 2013). However, these studies did not look at axial acceleration and instead used the axial tissue velocity data to track the mechanical wave. Furthermore, the in this study observed rapid sign change in the velocity and acceleration profiles in the first few milliseconds after stimulation were not reported by these studies. The low amplitude peaks in opposite direction in the velocity profile prior to the larger motion (i.e. the blue positive areas in the velocity panels of Fig. 4 and Fig. A1–3), were also reported by Nordez *et al.* (2009, see ref. Fig. 3). In the study of Nordez *et al.* this initial peak was absent in the distal portion of the muscle (i.e. close to the IZ) but prominent in the proximal part, comparable to the result shown in Fig. 4. The onset of large tissue motion was in all trials well after the onset of EMG activity, depicted in Fig. 4. In Grönlund *et al.* (2013) the large contraction motion was also succeeding the EMG activity, however EMG was recorded in separate trials prior to the ultrasound measurements.

Mechanical wave interpretation

In the current analysis, the axial tissue velocity and acceleration were used to track mechanical waves. The axial velocities do not directly reflect fiber elongation, but instead fiber thinning and thickening. Under the assumption that muscle fibers are incompressible (Fung, 2011), the shortening of a muscle fiber will increase its diameter. This complicates interpretation of the structural changes happening locally in the fiber during the contraction, as we are looking at a secondary effect. However, Lopata *et al.* (2010) found a high level of similarity in strain across longitudinal and axial directions during muscle contractions recorded at low frame rate with a 3D ultrasound transducer, indicating that axial deformations can be used as a measure for fiber elongation. Furthermore, the mechanical waves were detected with a velocity in the same range as the AP velocities. For these reasons, the mechanical waves are interpreted as contractile waves (ConW). The ConW is thought to depict the onset of local fiber motion, initiated by the arrival of the AP. This claim is further supported by the fact that the high amplitude motion occurs after AP arrival.

The AP and ConW arrival times (Table 2) do not reflect

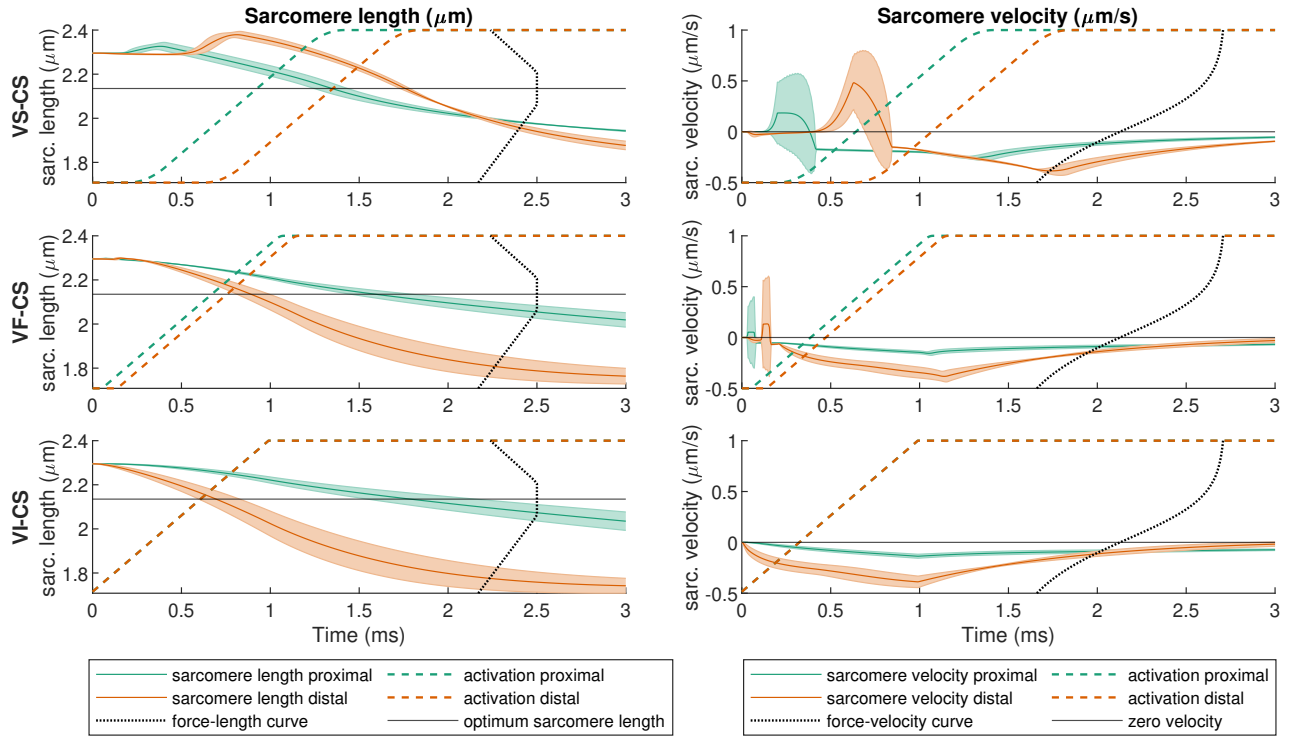

Fig. 7: Model simulation results show differences in proximal (first activated, green lines) and distal (orange lines) sarcomere lengths and velocities. Only results for the three strongly damped fiber designs are shown in this figure. **(Left column)** Sarcomere length nonuniformity between distal and proximal sarcomeres. Solid green lines denote mean length of the proximal sarcomeres, solid orange lines the mean length of the distal sarcomeres. The area surrounding the lines indicates the standard deviation. The dashed colored lines in matching color show the activation signal for the proximal and distal sarcomeres. The solid black line shows the sarcomere optimum length. The black dotted line shows the force-length function. **(Right column)** Sarcomere velocity nonuniformity between distal and proximal sarcomeres. Solid green lines denote mean velocity of the proximal sarcomeres, solid orange lines the mean velocity of the distal sarcomeres. The area surrounding the lines indicates the standard deviation. The dashed colored lines in matching color show the activation signal for the proximal and distal sarcomeres. The solid black line shows zero sarcomere velocity. The black dotted line shows the force-velocity function. **(Top row)** result for the slow action potential (V_SC_S), **(Middle row)**, result for fast action potential (V_FC_S) and **(Bottom row)** result for instantaneous activation (V_IC_S). In all cases, there is spread in sarcomere lengths and velocities. The spread is larger in the distal sarcomeres.

the full dynamics of the excitation-contraction (E-C) coupling, for two reasons. (1) The AP arrival was determined based on the spatio-temporal location of the depolarizing peak in the surface EMG recordings (denoted by the arrow in Fig. 3b). However, (surface) EMG reflects cellular calcium release initiated by the arrival of an AP (Röhrle *et al.* 2019), which on its turn initiates the formation of cross-bridges and thus force generation (i.e. the E-C coupling). Therefore, the actual moment of AP arrival and onset of local cross-bridge formation is earlier than the depolarizing peak, i.e. coinciding with the onset of EMG activity. (2) The peak in axial acceleration does not correspond to the onset of local contraction. The moment of motion onset is actually given by the onset in acceleration, and not the peak. However, detecting the onset of acceleration was not robust due to spatial variations in amplitude (depicted in Fig. A2). For these reasons, the differences in arrival times of AP and ConW currently do not give a complete characterization of the E-C timing.

In vivo: local sarcomere pulling

We observed a brief, low amplitude peak in the axial acceleration prior to the larger contractile motion, which is considered as a precontractile response (blue area in Fig. 4 and 5). This brief precontractile response was most obvious in tissue acceleration, but was also noticeable in tissue velocity (see Fig. 4 and A2). We hypothesize that this precontractile response is caused by earlier activated fiber segments, which will start to contract and pull on neighboring fiber segments. This pulling causes the neighboring (still inactive) fiber segments to elongate and thin. The pulling effect was in some trials observed prior to EMG onset, further indicating that this local motion is likely not caused by the active contraction of fiber segments at that location. A similar precontractile response was observed by Nordez *et al.* (2009, using UUI) and by Hufschmidt (1985, using a single stethoscope microphone). In both studies, this phenomenon was ascribed to latency relaxation (LR). LR was first observed by Rauh in 1922, and is described as a brief period in which the fiber tension momentarily drops, causing a muscle fiber to elongate prior to contracting (Sandow, 1952). LR has been measured extensively in isolated frog muscles, but recently Lindkvist *et al.* (2018) showed evidence of a similar precontractile response *in vivo* using near-infrared techniques. Using this optical technique a precontractile response temporally coinciding with the EMG activity was found. Since it is currently unknown how the ultrasound and optical response are linked, it remains elusive

whether the precontractile response detected in the tissue acceleration is indeed caused by LR, and corresponds to the optical response measured by Lindkvist *et al.* (2018). However, if LR causes a rapid drop in local fiber tension, this would result in a more clearly perceivable sarcomere pulling effect, supporting our hypothesis.

Experiment methodological considerations

Although longitudinal tissue velocities can be estimated, as shown by Grönlund *et al.* (2013) and Lopata *et al.* (2010), the spatial resolution in longitudinal direction is lower than the resolution in axial direction (Deffieux *et al.* 2008). RF-based speckle tracking in axial direction results in a sub-wavelength spatial resolution, whereas in longitudinal direction the resolution is dependent on the ultrasound element distance (typically in the order of one wavelength). Furthermore, there is no phase information available in the longitudinal direction. To detect the onset of fiber motion during the initial phase of contraction, the high temporal resolution provided by UUI is essential. There have been various studies combining conventional ultrasound imaging and HD-sEMG to study muscle contractions (e.g. Botter *et al.* 2013; Botter, 2019; Dieterich *et al.* 2017; Tweedell *et al.* 2019), however, our study has an unprecedented temporal resolution in simultaneous recording of EMG and ultrasound, caused by the use of UUI. It is expected that our method enables new research into the E-C coupling *in vivo*.

In the current study, a custom fitting procedure was used to estimate the velocity of the AP evoked by stimulation. In literature, typically motor unit action potential (MUAP) decomposition methods are used to estimate AP velocities (Florestal *et al.* 2006; Gligorijević *et al.* 2013; Holobar and Zazula, 2004). A MUAP from a single motor unit (MU) can be characterized by its unique shape and firing frequency, i.e. the MU's fingerprint. During a voluntary contraction, multiple MUs fire at different time instances, allowing decomposition of the recorded EMG signal into single MUAPs. Since the contraction in this study was evoked by electrical stimulation, the recorded EMG signal comprises the summation of multiple MU fingerprints that fire at the same moment. Hence, the unique temporal characteristic of the MUs is lost and decomposition methods are expected to fail. Therefore, the custom fitting procedure was used to estimate V_{ap} robustly. The parameters defined in the fit do not necessarily represent physiological parameters, due to the low complexity of the fitting model. For example, the delay term τ_{arr} defined in equation (3) was optimized to fit the data, and could also be negative. This does not mean that the measured EMG onsets prior to stimulation, but that the sine period and amplitude were fit on an AP with a right-skewed depolarizing peak, which the model could not explain. A future improvement for the fit could be the replacement of the sine with two asymmetric Gaussian functions.

For participant 1, the arrival time of the mechanical wave preceded the arrival time of the AP. This does not conflict with the presumption that these mechanical waves represent contractile waves, since this difference in arrival time seemingly resulted from the Radon tracking method. The wave tracking method could fit on either the first occurring peak (the presumed precontractile response), or on the higher amplitude, later occurring motion. In some trials this second motion was not a distinct peak, and therefore the Radon tracking method only detected the first peak. Further improvements in ultrasound data processing should be made to interpret the mechanical waves and to understand the physiological origin of the waves present during the onset of muscle contraction.

B. Fiber model simulation results

A micromechanical multisegmental fiber model was developed. The model allowed simulation of the local contractile response to a propagating AP, i.e. the propagation of the excitation-contraction (E-C) coupling. Considering the trend of the fiber contraction depicted in Fig. 6, the results were visually similar to those reported by Morgan *et al.* (1982). Morgan *et al.* modelled the fiber as 400 sarcomeres in series, with different initial lengths, and activated all sarcomeres simultaneously. The time to reach maximum force differs substantially between our results and those reported by Morgan *et al.* which can be explained by the parameters used in the model. Our parameters were not obtained by fitting the model on experimental data, but were taken from literature. The parameters that influenced the fiber contraction behaviour most were varied, i.e. nodal damping and AP velocity (Table 1). In all fiber designs, the weakly damped fibers reached higher velocities than the strongly damped fibers, which is an expected result. Likewise, the force in the weakly damped fibers did rise faster than the strongly damped fibers. The fiber with instantaneous activation had the lowest EMD, and the fiber with the slowest AP velocity had the highest EMD. As expected, all fiber designs converged to the same final whole fiber length, since the final whole fiber length was only dependent on the stiffness of the tendon, the initial length of the tendon and the maximum isometric force of a sarcomere. These properties were kept constant for all fiber designs.

Sarcomere length dispersion

Comparing the simulation results to other studies using multisegmental models (albeit with simultaneous sarcomere activation), we observed similar results in sarcomere length non-uniformities, i.e. dispersion (Campbell, 2009; Morgan *et al.* 1982; Stoecker *et al.* 2009). In our study, the sarcomere length dispersions were observed for all AP velocities. Furthermore, we observed a difference in the sarcomere length distribution between proximal and distal sarcomeres. Although this has not been shown explicitly in simulation studies, Moo and Herzog (2018) measured similar non-uniformities in sarcomere length (i.e. SL dispersions) *in vivo* during mice tibialis-anterior muscle contractions. It was found that SL dispersion was up to $1.0\,\mu\text{m}$ for 30 serial sarcomeres. In addition, it was found that the sarcomeres at the distal end of the muscle elongated more than the sarcomeres in the middle of the muscle. Though these results are not directly comparable

to the difference in proximal and distal sarcomere lengths in our simulations, it does highlight that sarcomere length varies locally in a fiber, i.e. within 30 sarcomeres in series, and further along the fiber.

In silico: Local sarcomere pulling

Upon closer examination of the sarcomere lengths during the initial phase of the contraction, we can see that some sarcomeres are first elongated prior to contracting. This happens in more distal sarcomeres and is caused by a pulling force of proximal sarcomeres that are activated earlier, similar to the local pulling effect observed in the experiment. The pulling effect is most prominent in the fiber with the slow AP, but also present in the fiber with the fast AP, as can be seen in the velocity traces in Fig. 7 (and Fig. A4). Furthermore, the effect is stronger in the weakly damped fibers, which can be expected since the boundaries in this fiber can move more fluidly. A similar initial elongation of sarcomeres was seen by Stoecker *et al.* (2009, see ref. Fig. 3), though the authors did not explicitly address this phenomenon since their interest was on a longer time scale (up to multiple seconds).

A direct consequence of the local sarcomere elongation prior to contraction is the build-up of passive tension in the fiber. The force generated by actively contracting sarcomeres is first stored as elastic energy in the passive elastic connective tissue, and is later released in the form of kinetic energy. This additional step makes the fiber slower, and was most obvious in the $\mathtt{V_SC_W}$ fiber. Another observation is that there is negative work done by sarcomeres that are elongated prior to contracting. As the elongating sarcomeres are first gaining eccentric velocity, this velocity first has to be reversed to start contracting. Due to the low inertia of the fiber, this happens quickly. In most fiber designs, this negative work was done predominantly by the passive tissue, however, in the $\mathtt{V_SC_W}$ fiber also the active sarcomere force contributed to the negative work done. This local negative power output was also present in the multisegmental model of Van Leeuwen and Kier (1997). This effect can only be seen in multisegmental models, since these local sarcomere interactions cannot be studied in single contractile element models.

Another effect of this local pulling is that the sarcomeres are first being pulled more towards the descending limb of the force-length relation in the Hill model. This causes a decrease in the active force generating capacity of the sarcomere when it starts to be activated (see black dashed line in Fig. 7). When considering only the static case, this would indeed decrease the contraction efficiency of the fiber. However, in the dynamic case, the eccentric velocity the individual sarcomeres gained increases the value of the force-velocity relation defined in the Hill model, thereby enhancing the force generating capacity of the fiber. As such, the Hill model makes it difficult to interpret what exactly is happening locally in the fiber concerning contraction efficiency.

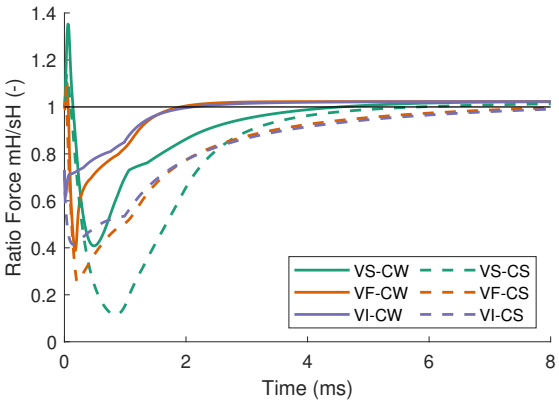

Fig. 8: Ratio between the force predicted by a single Hill (sH) element muscle fiber versus a multisegmental Hill (mH) muscle fiber. The input to the sH model was the whole fiber length and velocity obtained in the mH model simulations. The activation of the sH model was chosen as the mean activation over all sarcomeres in the mH model per time step. It can be seen that during the initial transient phase of the contraction, the mH model underestimates the force predicted by the sH model. After some time, the mH model converge to the same force as the sH model. This indicates that the initial transient in the mH model needs to be validated in a different way.

Model validation

It is challenging to validate the proposed model. The simulation time for the model is highly dependent on the number of sarcomeres in series, but also on the amount of damping in the model (simulation time varying from 1 to up to 15 hours per simulation). Therefore, validating the model by fitting to experimental data is currently not feasible. Instead, a single segment Hill model served as validation. Looking at the ratio of force in the multisegmental Hill model (mH) over the force in the single Hill (sH) model, we see that both models have different behaviours during the onset of contraction (Fig. 8). However, both models converge to the same force after an initial transient. This validates the model only from the moment that uniform activation is reached. Further validation for the initial transient is needed, although our experimental results visually show a similar phenomenon, i.e. the earlier discussed local pulling effect. Recent developments in optical techniques can provide additional data of *in vivo* sarcomere lengths during twitch contractions to further validate the model (Lichtwark *et al.* 2018; Moo and Herzog, 2018; Sanchez *et al.* 2015; Young *et al.* 2017).

Model methodological considerations

The proposed model structure represents a single muscle fiber. Consequently, only series pathway force transmission can be studied, since fiber interactions could not be included. In the single fiber simulations, high contractile velocities and accelerations were observed, which are unlikely to occur in whole muscles. Increasing the density of the sarcomeres did limit the rapid velocity changes, but did not alter the general behaviour (i.e. the local pulling effect was still present). A whole muscle consists of fascicles and fascicles consist of multiple fibers in parallel. These fibers have interconnections and are surrounded by connective

tissue, resulting in various force transmission pathways (Patel and Lieber, 1997). A next step with this model would be to add multiple fibers in parallel, to further study the transmission of force during the onset of muscle contraction. The added fibers will also increase the inertia in the system, limiting the high accelerations seen in the present model.

C. Implications

Both experiment and simulations resulted in data that indicates local pulling of sarcomeres during the onset of contraction. It is currently uncertain whether the simulated data and the experimental data show the same phenomenon. The model simulated only a single fiber, hence no interactions with other fibers and connective tissue were considered. However, due to the fact that electrically evoked contractions were used, it is not unlikely that the local pulling effect was present *in vivo* and *in silico*.

Latency relaxation (LR) in single muscle fibers has been shown extensively in previous studies (Sandow, 1952). In voluntary contractions, the effect of LR on whole muscle length during contraction is expected to be negligible, since MUs fire with different frequencies and at different time instances. It is likely that individual fibers that are 'relaxing' do not significantly alter the whole muscle behaviour, since there are sufficient fibers to compensate for this momentarily local 'relaxation'. However, when electrically stimulating the muscle, all fibers are excited at the same time, likely amplifying the effect caused by LR. This possibly results in the observations presented in this study. It should be noted that the similar behaviour in sarcomere pulling seen *in silico* cannot be originated by LR, since LR is not described in the Hill model.

If LR would be implemented in an adapted version of the Hill model, we expect that the local pulling effect will be stronger. In the current simulations, the tension rises due to the local pulling effect, caused by the passive length-tension relation. This contradicts findings of LR in single fiber experiments, and shows that the phenomenological Hill model is not best suited for studying the E-C propagation. A future improvement of the model would be to make a more distinct separation in contributions of active muscle tissue and passive connective tissue. As such, a physiological model instead of a phenomenological model would be better suited to make such separation, at the cost of computational complexity (Campbell, 2009; Huxley, 1974; Lemaire *et al.* 2016).

The current study highlights that there are many unknowns in what happens locally in muscle fibers when the AP arrives, and how the fiber will respond locally to this excitation, i.e. the local E-C coupling. The presented novel method to image the E-C propagation seems promising to further investigate local fiber behaviour. The method needs to be standardized, and used to characterize the influence of various experimental conditions, such as the effect of joint position (i.e. effect of initial passive pre-tension and sarcomere length), the effect of stimulation current and the effect of measurement location with respect to the innervation zone. The here presented results and those of previous studies highlight that assuming a uniform sarcomere length and activation over the whole muscle is likely to result in erroneous prediction of muscle behaviour during contractions, especially during rapid transients (Moo and Herzog, 2018). Ultimately, the proposed experimental method can bridge the gap in fiber behaviour at the micro scale, and whole muscle behaviour at the macro scale (Campbell, 2009). Combining experimental protocols that measure (1) micro-scale sarcomere lengths over time, (2) macro-scale joint level movement and muscle forces and (3) meso-scale propagation of contractile waves is needed to integrate all observations and further the domain of multisegmental muscle modelling.

Outlook: Clinical implementation

In order to translate the method to the clinic, the method first needs to be standardized and more thoroughly evaluated in healthy participants. Because of ethical considerations when testing patients, preferably the electrostimulation is substituted by voluntary contractions. Tracking electromechanical muscle dynamics in voluntary contractions imposes new challenges. First, in voluntary contractions, multiple MUs are involved, firing at different time instants with different frequencies. Therefore, it can be expected that there is not a distinct motion onset like with electrostimulation, but rather a gradually increasing motion consisting of many waves caused by the multiple recruited muscle fibers. This can be seen as a compound wave. Previous studies that determined muscle contraction onset in voluntary contractions using M-mode ultrasound and EMG resulted in findings that are contradicting E-C theory (Dieterich *et al.* 2017; Tweedell *et al.* 2019). It was found that M-mode ultrasound detected contraction onset earlier than EMG (full-wave rectified). These contradicting results can be ascribed to two causes, (1) time synchronization issues with clinical ultrasound scanners and (2) lack of sensitive measurement and processing methods. The contradicting results underline the challenge in analyzing data from voluntary contractions.

To overcome the challenges of tracking the E-C coupling in voluntary contractions, new processing techniques need to be developed. To characterize the E-C coupling on single MU level, decomposition techniques similar to those used for EMG decomposition may be needed. This would allow to decompose the compound mechanical wave into the mechanical waves per MU, e.g. by using the decomposed EMG as prior information. However, less advanced analysis methods may result in relevant clinical information in the near future. Performing frequency analysis on compound wave and EMG data from voluntary contractions may lead to new insights into the relation between the excitation and contraction waves.

On the other hand, electrical stimulation has been used to evoked muscle contractions in patient studies (Lacourpaille *et al.* 2017, 2014). Using our proposed method to measure pathological muscle can lead to new insights in the pathophysiology of neuromuscular diseases. Possible metrics are the velocities of AP and ConW, the

spatio-temporal characteristics of these waves and possible inhomogeneity in the mechanical wave pattern.

V. Conclusions

- The novel experimental method to track electromechanical dynamics in skeletal muscle with high spatio-temporal resolution successfully detected propagating mechanical waves in response to propagating excitation waves (i.e. action potentials).
- The newly developed multisegmental fiber model allowed to simulate the contractile response to a propagating excitation wave. Simulated fiber contractions showed similar results as the experiment, but extensive validation of the model during the onset of contraction is needed.
- Both the experiment and simulation resulted in precontractile motion that may be caused by earlier activated sarcomeres that pull on sarcomeres that were not yet excited. This effect was presumably amplified in the experiment by latency relaxation.
- Although many questions remain about the onset of muscle contraction, we showed a promising new technique that can provide additional data needed to integrate micro-scale and macro-scale measurements, and further our understanding of muscle behaviour.

Acknowledgment

I would first like to thank my supervisors, Winfred Mugge, Alfred Schouten and Verya Daeichin for their guidance, feedback and the interesting discussions throughout the project. I would like to thank Henry den Bok, Ronald Ligteringen, Thim Zuidwijk, Sven Kraaijevanger and Elias Mateo Fernandez for their technical support. Furthermore, I would like to thank Jurriaan de Groot, Hermien Kan, Erik Niks and Fabian Kerkhof for their input regarding clinical relevance of the project. And finally, I would like to express my gratitude to Rik Vos, Nico de Jong, Jason Voorneveld, Annette Caenen, Martin Verweij and Hans Bosch for their input on the ultrasound acquisition, processing and analysis.

References

Barbero, Marco, Roberto Merletti, and Alberto Rainoldi (2012). *Atlas of Muscle Innervation Zones: Understanding Surface Electromyography and Its Applications*. Milan ; New York: Springer.

Botter, A., T. M. M. Vieira, I. D. Loram, R. Merletti, and E. F. Hodson-Tole (2013). "A Novel System of Electrodes Transparent to Ultrasound for Simultaneous Detection of Myoelectric Activity and B-Mode Ultrasound Images of Skeletal Muscles". In: *Journal of Applied Physiology* 115.8, pp. 1203–1214.

Botter, Alberto (2019). "Integration of HD-sEMG and Ultrasounds for the Assessment of Muscle Function". In: *Converging Clinical and Engineering Research on Neurorehabilitation III*. Ed. by Lorenzo Masia, Silvestro Micera, Metin Akay, and José L. Pons. Vol. 21. Cham: Springer International Publishing, pp. 1152–1155.

Campbell, Kenneth S. (2009). "Interactions between Connected Half-Sarcomeres Produce Emergent Mechanical Behavior in a Mathematical Model of Muscle". In: *PLOS Computational Biology* 5.11, e1000560.

Cavanagh, P. R. and P. V. Komi (1979). "Electromechanical Delay in Human Skeletal Muscle under Concentric and Eccentric Contractions". In: *Europ. J. Appl. Physiol.* 42.3, pp. 159–163.

Claflin, Dennis R. and Susan V. Brooks (2008). "Direct Observation of Failing Fibers in Muscles of Dystrophic Mice Provides Mechanistic Insight into Muscular Dystrophy". In: *American Journal of Physiology-Cell Physiology* 294.2, pp. C651–C658.

Deffieux, T., J. Gennisson, M. Tanter, and M. Fink (2008). "Assessment of the Mechanical Properties of the Musculoskeletal System Using 2-D and 3-D Very High Frame Rate Ultrasound". In: *IEEE Transactions on Ultrasonics, Ferroelectrics, and Frequency Control* 55.10, pp. 2177–2190.

Deffieux, Thomas, Jean-Luc Gennisson, Mickaël Tanter, Mathias Fink, and Antoine Nordez (2006). "Ultrafast Imaging of in Vivo Muscle Contraction Using Ultrasound". In: *Appl. Phys. Lett.* 89.18, p. 184107.

Dieterich, Angela V., Alberto Botter, Taian Martins Vieira, Anneli Peolsson, Frank Petzke, Paul Davey, and Deborah Falla (2017). "Spatial Variation and Inconsistency between Estimates of Onset of Muscle Activation from EMG and Ultrasound". In: *Scientific Reports* 7, p. 42011.

Farina, Dario, Andrea Blanchietti, Marco Pozzo, and Roberto Merletti (2004). "M-Wave Properties during Progressive Motor Unit Activation by Transcutaneous Stimulation". In: *Journal of Applied Physiology* 97.2, pp. 545–555.

Florestal, J. R., P. A. Mathieu, and A. Malanda (2006). "Automated Decomposition of Intramuscular Electromyographic Signals". In: *IEEE Transactions on Biomedical Engineering* 53.5, pp. 832–839.

Fung, Y. C (2011). *Biomechanics: Mechanical Properties of Living Tissues*. New York: Springer.

Gillies, Allison R. and Richard L. Lieber (2011). "Structure and Function of the Skeletal Muscle Extracellular Matrix". In: *Muscle Nerve* 44.3, pp. 318–331.

Gligorijević, Ivan, Johannes P. van Dijk, Bogdan Mijović, Sabine Van Huffel, Joleen H. Blok, and Maarten De Vos (2013). "A New and Fast Approach towards sEMG Decomposition". In: *Medical & Biological Engineering & Computing* 51.5, pp. 593–605.

Grönlund, Christer, Kenji Claesson, and Andreas Holtermann (2013). "Imaging Two-Dimensional Mechanical Waves of Skeletal Muscle Contraction". In: *Ultrasound in Medicine & Biology* 39.2, pp. 360–369.

Günther, Michael, Oliver Röhrle, Daniel FB Haeufle, and Syn Schmitt (2012). "Spreading out Muscle Mass within a Hill-Type Model: A Computer Simulation Study". In: *Computational and mathematical methods in medicine* 2012.

Hill, Archibald Vivian (1953). "The Mechanics of Active Muscle". In: *Proceedings of the Royal Society of London. Series B-Biological Sciences* 141.902, pp. 104–117.

Holobar, A. and D. Zazula (2004). "Correlation-Based Decomposition of Surface Electromyograms at Low Contraction Forces". In: *Medical & Biological Engineering & Computing* 42.4, pp. 487–495.

Hu, X., B. Afsharipour, W. Z. Rymer, and N. L. Suresh (2016). "Impairment of Muscle Force Transmission in Spastic-Paretic Muscles of Stroke Survivors". In: *2016 38th Annual International Conference of the IEEE Engineering in Medicine and Biology Society (EMBC)*, pp. 6098–6101.

Hufschmidt, A. (1985). "Acoustic Phenomena in the Latent Period of Skeletal Muscle: A Simple Method for in-Vivo Measurement of the Electro-Mechanic Latency (EML)". In: *Pflugers Arch.* 404.2, pp. 162–165.

Hug, François, Kylie Tucker, Jean-Luc Gennisson, Mickaël Tanter, and Antoine Nordez (2015). "Elastography for Muscle Biomechanics: Toward the Estimation of Individual Muscle Force". In: *Exercise and Sport Sciences Reviews* 43.3, p. 125.

Huxley, A F (1974). "Muscular Contraction." In: *The Journal of Physiology* 243.1, pp. 1–43.

Huxley, Andrew F. (1957). "Muscle Structure and Theories of Contraction". In: *Prog. Biophys. Biophys. Chem* 7, pp. 255–318.

Lacourpaille, Lilian, Raphaël Gross, François Hug, Arnaud Guével, Yann Péréon, Armelle Magot, Jean-Yves Hogrel, and Antoine Nordez (2017). "Effects of Duchenne Muscular Dystrophy on Muscle Stiffness and Response to Electrically-Induced Muscle Contraction: A 12-Month Follow-Up". In: *Neuromuscular Disorders* 27.3, pp. 214–220.

Lacourpaille, Lilian, François Hug, Arnaud Guével, Yann Péréon, Armelle Magot, Jean-Yves Hogrel, and Antoine Nordez (2014). "New Insights on Contraction Efficiency in Patients with Duchenne Muscular Dystrophy". In: *Journal of Applied Physiology* 117.6, pp. 658–662.

Lacourpaille, Lilian, François Hug, and Antoine Nordez (2013a). "Influence of Passive Muscle Tension on Electromechanical Delay in Humans". In: *PLoS ONE* 8.1. Ed. by Christof Markus Aegerter, e53159.

Lacourpaille, Lilian, Antoine Nordez, and François Hug (2013b). "Influence of Stimulus Intensity on Electromechanical Delay and Its Mechanisms". In: *Journal of Electromyography and Kinesiology* 23.1, pp. 51–55.

Le, Shimin, Miao Yu, Ladislav Hovan, Zhihai Zhao, James Ervasti, and Jie Yan (2018). "Dystrophin As a Molecular Shock Absorber". In: *ACS Nano* 12.12, pp. 12140–12148.

Lemaire, Koen K., Guus C. Baan, Richard T. Jaspers, and A. J. 'Knoek' van Soest (2016). "Comparison of the Validity of Hill and Huxley Muscle–Tendon Complex Models Using Experimental Data Obtained from Rat m. Soleus in Situ". In: *Journal of Experimental Biology* 219.7, pp. 977–987.

Lichtwark, Glen A., Dominic J. Farris, Xuefeng Chen, Paul W. Hodges, and Scott L. Delp (2018). "Microendoscopy Reveals Positive Correlation in Multiscale Length Changes and Variable Sarcomere Lengths across Different Regions of Human Muscle". In: *Journal of Applied Physiology* 125.6, pp. 1812–1820.

Lindkvist, Markus, Gabriel Granåsen, and Christer Grönlund (2018). "Precontractile Optical Response during Excitation-Contraction in Human Muscle Revealed by Non-Invasive High-Speed Spatiotemporal NIR Measurement". In: *Scientific Reports* 8.1.

Lopata, Richard G. P., Johannes P. van Dijk, Sigrid Pillen, Maartje M. Nillesen, Huub Maas, Johan M. Thijssen, Dick F. Stegeman, and Chris L. de Korte (2010). "Dynamic Imaging of Skeletal Muscle Contraction in Three Orthogonal Directions". In: *Journal of Applied Physiology* 109.3, pp. 906–915.

Merletti, R., A. Fiorito, L. R. Lo Conte, and C. Cisari (1998). "Repeatability of Electrically Evoked EMG Signals in the Human Vastus Medialis Muscle". In: *Muscle & Nerve* 21.2, pp. 184–193.

Moo, Eng Kuan and Walter Herzog (2018). "Single Sarcomere Contraction Dynamics in a Whole Muscle". In: *Sci Rep* 8.1, pp. 1–10.

Morgan, D.L., S. Mochon, and F.J. Julian (1982). "A Quantitative Model of Intersarcomere Dynamics during Fixed-End Contractions of Single Frog Muscle Fibers". In: *Biophysical Journal* 39.2, pp. 189–196.

Moritani, T., D. Stegeman, and R. Merletti (2004). "Basic Physiology and Biophysics of EMG Signal Generation". In: *Electromyography Physiology Engineering and Noninvasive Applications*, pp. 1–20.

Nordez, Antoine, Thomas Gallot, Stefan Catheline, Arnaud Guével, Christophe Cornu, and François Hug (2009). "Electromechanical Delay Revisited Using Very High Frame Rate Ultrasound". In: *Journal of Applied Physiology* 106.6, pp. 1970–1975.

Patel, T. J. and R. L. Lieber (1997). "Force Transmission in Skeletal Muscle: From Actomyosin to External Tendons." In: *Exerc Sport Sci Rev* 25, pp. 321–363.

Röhrle, Oliver, Utku Ş. Yavuz, Thomas Klotz, Francesco Negro, and Thomas Heidlauf (2019). "Multiscale Modeling of the Neuromuscular System: Coupling Neurophysiology and Skeletal Muscle Mechanics". In: *Wiley Interdisciplinary Reviews: Systems Biology and Medicine* 11.6.

Sanchez, Gabriel N., Supriyo Sinha, Holly Liske, Xuefeng Chen, Viet Nguyen, Scott L. Delp, and Mark J. Schnitzer (2015). "In Vivo Imaging of Human Sarcomere Twitch Dynamics in Individual Motor Units". In: *Neuron* 88.6, pp. 1109–1120.

Sandow, Alexander (1952). "Excitation-Contraction Coupling in Muscular Response". In: *Yale J Biol Med* 25.3, pp. 176–201.

Stegeman, Dick F., Bert U. Kleine, Bernd G. Lapatki, and Johannes P. Van Dijk (2012). "High-Density Surface EMG: Techniques and Applications at a Motor Unit Level". In: *Biocybernetics and biomedical engineering* 32.3, pp. 3–27.

Stegeman, Dick F, Joleen H Blok, Hermie J Hermens, and Karin Roeleveld (2000). "Surface EMG Models: Properties and Applications". In: *Journal of Electromyography and Kinesiology* 10.5, pp. 313–326.

Stoecker, Urs, Ivo A. Telley, Edgar Stüssi, and Jachen Denoth (2009). "A Multisegmental Cross-Bridge Kinetics Model of the Myofibril". In: *Journal of Theoretical Biology* 259.4, pp. 714–726.

Tweedell, Andrew J., Matthew S. Tenan, and Courtney A. Haynes (2019). "Differences in Muscle Contraction Onset as Determined by Ultrasound and Electromyography". In: *Muscle & Nerve* 59.4, pp. 494–500.

Van Leeuwen, J. L. and W. M. Kier (1997). "Functional Design of Tentacles in Squid: Linking Sarcomere Ultrastructure to Gross Morphological Dynamics". In: *Philosophical Transactions of the Royal Society of London. Series B: Biological Sciences* 352.1353, pp. 551–571.

Vos, Hendrik J., Bas M. van Dalen, Ilkka Heinonen, Johan G. Bosch, Oana Sorop, Dirk J. Duncker, Antonius F. W. van der Steen, and Nico de Jong (2017). "Cardiac Shear Wave Velocity Detection in the Porcine Heart". In: *Ultrasound in Medicine & Biology* 43.4, pp. 753–764.

Yekutieli, Yoram, Roni Sagiv-Zohar, Ranit Aharonov, Yaakov Engel, Binyamin Hochner, and Tamar Flash (2005). "Dynamic Model of the Octopus Arm. I. Biomechanics of the Octopus Reaching Movement". In: *Journal of Neurophysiology* 94.2, pp. 1443–1458.

Young, Kevin W., Bill P. -P. Kuo, Shawn M. O'Connor, Stojan Radic, and Richard L. Lieber (2017). "In Vivo Sarcomere Length Measurement in Whole Muscles during Passive Stretch and Twitch Contractions". In: *Biophysical Journal* 112.4, pp. 805–812.

Yucesoy, Can A., Bart H. F. J. M. Koopman, Peter A. Huijing, and Henk J. Grootenboer (2002). "Three-Dimensional Finite Element Modeling of Skeletal Muscle Using a Two-Domain Approach: Linked Fiber-Matrix Mesh Model". In: *Journal of Biomechanics* 35.9, pp. 1253–1262.

Appendix A
Additional results

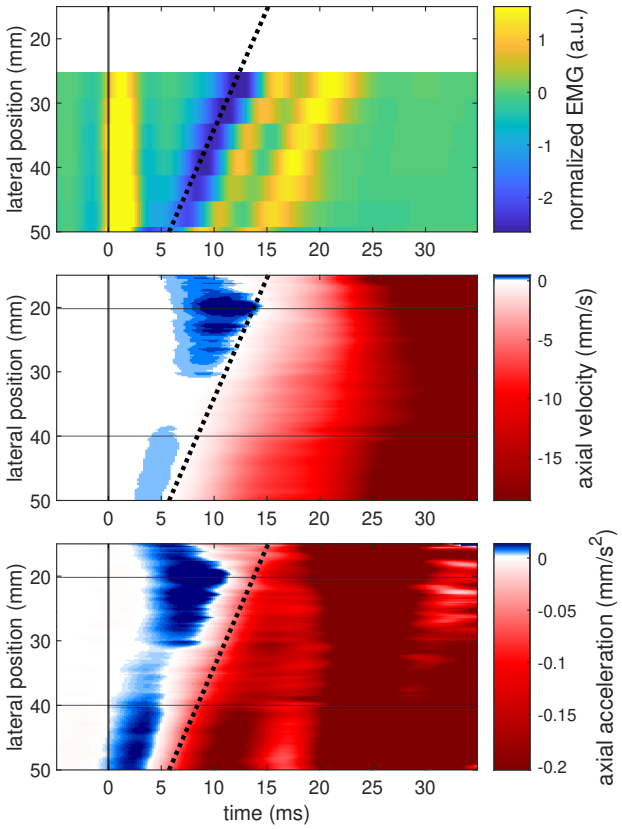

Fig. A1: Typical result for participant 1, M-mode at depth 10 mm. **(Top)** EMG of column beneath ultrasound probe. Velocity of the action potential $V_{\text{ap}} = 3.73\,\text{m}\,\text{s}^{-1}$. The black dotted line denotes the depolarizing peak in the EMG signal in every panel. The yellow peak at $t = 0\,\text{ms}$ is a stimulation artifact. **(Center)** axial tissue velocity along the M-mode. **(Bottom)** axial tissue acceleration. It can be seen that the blue area in the tissue velocity and tissue acceleration precedes the depolarizing peak in EMG, and has a slope very similar to the black dotted line fitted through the depolarizing peak. The velocities arrival times for participant 1 listed in Table 2 were in some trials fitted on the first blue wave, and in some trials on a red wave. In this trial, this would be the wave between 5 and 15 ms, but this wave could not be found with the Radon tracking method since it is not as outstanding as the blue wave.

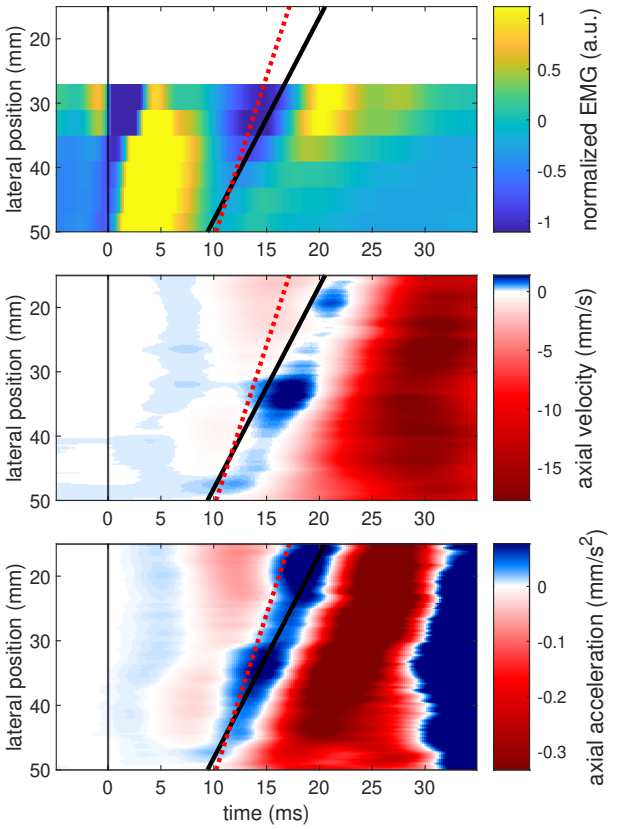

Fig. A2: Another typical result for participant 2, different trial then Fig. 4, M-mode at depth 12 mm. **(Top)** EMG of column beneath ultrasound probe. Velocity of the action potential $V_{\text{ap}} = 5.04\,\text{m}\,\text{s}^{-1}$. The red dotted line denotes the depolarizing peak in the EMG signal in every panel. The yellow peak at $t = 0\,\text{ms}$ is a stimulation artifact. **(Center)** axial tissue velocity along the M-mode. **(Bottom)** axial tissue acceleration. It can be seen that the blue area in the tissue velocity and tissue acceleration temporally coincides with the depolarizing peak in EMG, and has a slope very similar to the black line fitted through the depolarizing peak. The contractile wave was tracked resulting in $V_{\text{conw}} = 3.15\,\text{m}\,\text{s}^{-1}$ and arrival time $T_{\text{arr-conw}} = 9.41\,\text{ms}$.

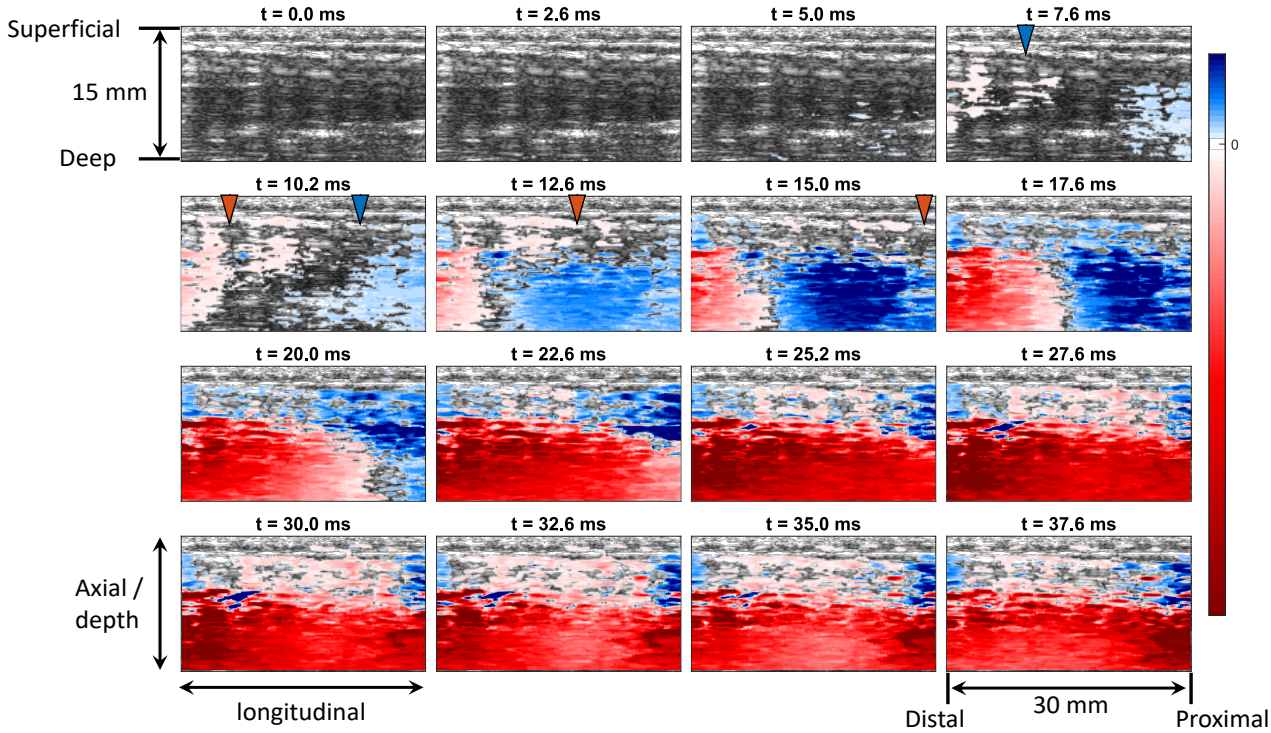

Fig. A3: Typical result of axial tissue velocity over time for participant 2. Blue denotes positive (upwards) and red negative (downward) velocity. The blue triangle at the top of a panel denotes the onset of EMG activity, propagating from distal to proximal. The red triangle denotes the depolarizing peak in EMG activity. From 10 ms positive velocity propagates from left to right (i.e. distal to proximal). This blue area is immediately followed by a higher amplitude negative velocity (red area).

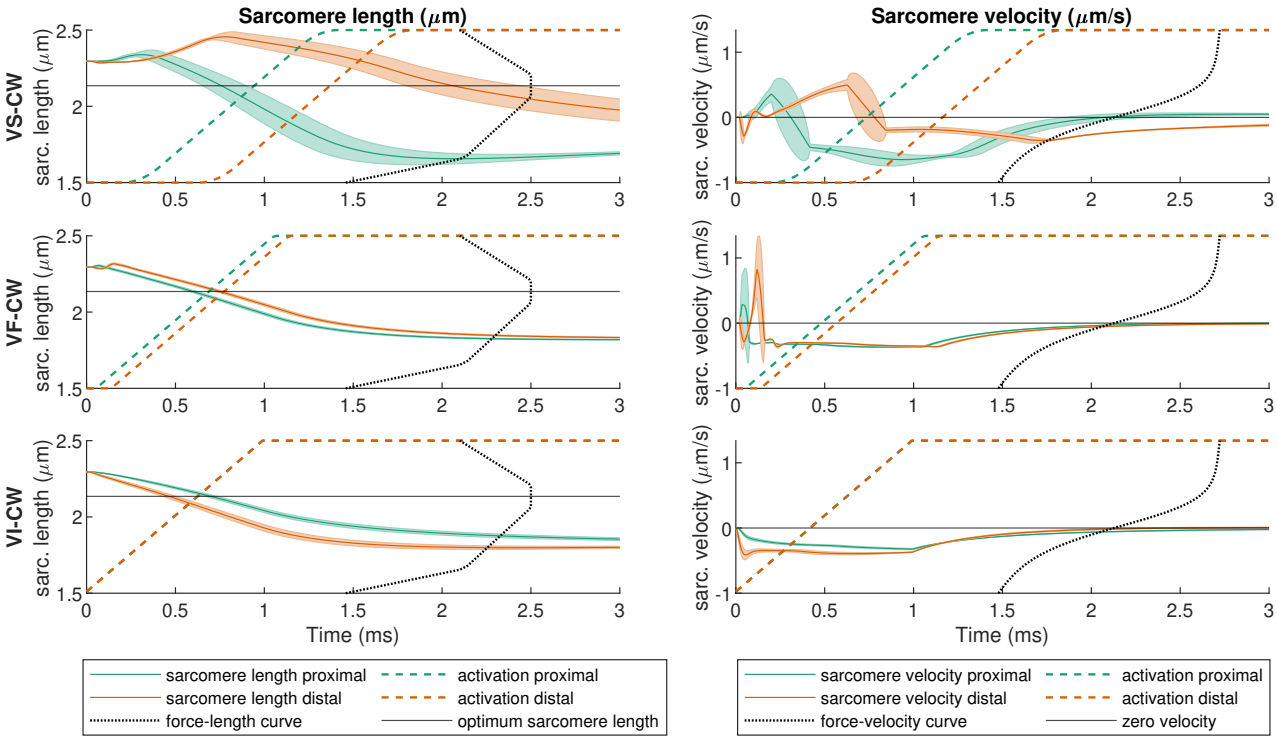

Fig. A4: Model simulation results show differences in proximal (first activated, green lines) and distal (orange lines) sarcomere lengths and velocities. Only results for the three weakly damped fiber designs are shown in this figure. **(Left column)** Sarcomere length nonuniformity between distal and proximal sarcomeres. Solid green lines denote mean length of the proximal sarcomeres, solid orange lines the mean length of the distal sarcomeres. The area surrounding the lines indicates the standard deviation. The dashed colored lines in matching color show the activation signal for the proximal and distal sarcomeres. The solid black line shows the sarcomere optimum length. The black dotted line shows the force-length function. **(Right column)** Sarcomere velocity nonuniformity between distal and proximal sarcomeres. Solid green lines denote mean velocity of the proximal sarcomeres, solid orange lines the mean velocity of the distal sarcomeres. The area surrounding the lines indicates the standard deviation. The dashed colored lines in matching color show the activation signal for the proximal and distal sarcomeres. The solid black line shows zero sarcomere velocity. The black dotted line shows the force-velocity function. **(Top row)** result for the slow action potential ($\mathrm{V_S C_W}$), **(Middle row)**, result for fast action potential ($\mathrm{V_F C_W}$) and **(Bottom row)** result for instantaneous activation ($\mathrm{V_I C_W}$). In all cases, there is spread in sarcomere lengths and velocities. The spread is larger in the distal sarcomeres.

Appendix B
Micromechanical Fiber Model

The muscle fiber is modelled as a large chain of n sarcomeres in series. The force in sarcomere i is described by the Hill model, relating the sarcomere length ℓ_i, velocity $\dot{\ell}_i$ and activation a_i to force $F_{\mathrm{s},i}$. The sarcomeres are separated by boundaries, i.e. Z-disks, which are represented by a 1D array of $m = n + 1$ point masses, where boundary j has position x_j. The first boundary is fixed, and the last boundary x_n is connected to a tendon, modelled as a linear spring. The position of the other end of the tendon is given by x_t, and is fixed during muscle contraction. A schematic overview of the model is depicted in Fig. B5. Throughout the model description, the following notation is used,

x	a scalar
$\boldsymbol{x}$	a vector
$\mathbf{X}$	a matrix
x_i	an element in a vector
$\dot{x}, \ddot{x}$	time derivatives of x

An overview of the model parameters is given in Table B1.

A. Assumptions

In our model of the muscle, the following assumptions are introduced to simplify the system.

(a) All sarcomeres have identical properties. It is known that the sarcomere optimum length varies across muscle fibers, but in the model it is assumed that all sarcomeres have the same optimum length. This is justified by modelling a small portion of the fiber, i.e. 500 sarcomeres. As such, we expect a minor influence of nonuniform optimum sarcomere length at this scale.

(b) We consider a single fiber, and therefore no fiber interactions can be considered. It is assumed that a fiber segment consists of a single myofibril, and a myofibril consists of a single sarcomere. Consequently, within the fiber only series pathway force transmission is modelled. By modelling only a single fiber, also inter-fiber lateral force transmission as has been described by Huijing (1999) is omitted.

(c) The electrophysiology is assumed to be unaffected by contraction. The modelled fiber is short, so displacements between start of local activation and full activation are expected to be small.

(d) Muscle tissue is viscoelastic, however, viscous effects are in general not considered in Hill model (Hill, 1953). These viscoelastic effects can be of great influence in experiments on the millisecond scale. Therefore, we added a linear damper, corresponding to passive viscoelastic properties, as have been reported by e.g. Gordon *et al.* (1966). This also helped the numerical integration of the model, reducing oscillations. Two kinds of damping were implemented, relative damping (using the relative velocity of the sarcomeres and tendon) and nodal damping (using the velocities of the boundaries in the model). In the current study, the relative damping is set to zero.

(e) Muscle tissue is often modelled as incompressible (Fung, 2011), and therefore we assume a constant volume sarcomere. No additional forces caused by intra-sarcomere pressure due to volume constant constrained were considered, since this is already incorporated in the passive strain-tension relation on whole muscle scale. Furthermore, it is unknown on what scale the incompressibility assumptions is valid, since the authors do not know whether the Z-disks separating sarcomeres are permeable.

B. Model geometry and kinematics

The position $\boldsymbol{x}(t)$ and velocity $\dot{\boldsymbol{x}}(t)$ of the m sarcomere boundaries over time are given by the vectors,

$$\boldsymbol{x}(t) = \begin{pmatrix} x_1(t) & x_2(t) & \dots & x_m(t) \end{pmatrix}^T, \tag{B.1}$$

$$\dot{\boldsymbol{x}}(t) = \begin{pmatrix} \dot{x}_1(t) & \dot{x}_2(t) & \dots & \dot{x}_m(t) \end{pmatrix}^T. \tag{B.2}$$

Similarly, the length of n sarcomeres over time is given by the vector,

$$\boldsymbol{\ell}(t) = \begin{pmatrix} \ell_1(t) & \ell_2(t) & \dots & \ell_n(t) \end{pmatrix}^T. \tag{B.3}$$

The sarcomere boundaries are chosen as generalized coordinates in the model, and as such, the sarcomere length, velocity and acceleration can be determined from the boundary positions using,

$$\ell_i(t) = x_{i+1}(t) - x_i(t), \tag{B.4}$$

$$\dot{\ell}_i(t) = \dot{x}_{i+1}(t) - \dot{x}_i(t), \tag{B.5}$$

$$\ddot{\ell}_i(t) = \ddot{x}_{i+1}(t) - \ddot{x}_i(t). \tag{B.6}$$

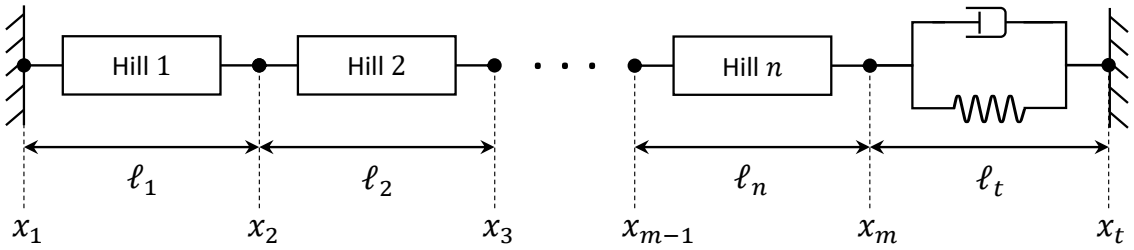

Fig. B5: Schematic representation of the fiber model. The fiber consists of n Hill models in series, each representing a sarcomere with length $\ell_i(t)$ over time t, where i denotes the sarcomere number. Sarcomeres are separated by boundaries with position $x_j(t)$. On the proximal end (first activated, low numbers) the first sarcomere is attached to the fixed world. On the distal end, the last sarcomere is attached to a viscoelastic tendon, represented by a spring-damper element.

The longitudinal nominal sarcomere strain is given by,

$$\varepsilon_i(t) = \left(\ell_i(t) - \ell_{\text{optim},i}\right)/\ell_{\text{optim},i}, \tag{B.7}$$

where $\ell_{\text{optim},i}$ is the optimum sarcomere length. The longitudinal sarcomere strain rate is given by,

$$\dot{\varepsilon}_i(t) = \dot{\ell}_i(t)/\ell_{\text{optim},i}. \tag{B.8}$$

Throughout the model description, the low numbered boundaries and sarcomeres will be referred to as the proximal end of the fiber, and the high numbered boundaries and sarcomeres will be referred to as the distal end of the fiber. In the following, the time dependency (t) will be omitted for simplicity of the equations.

C. Sarcomere force

The force in the sarcomere is described by the Hill model (Gordon *et al.* 1966; Hill, 1953). In the Hill model, the force in a muscle is divided in three lumped components, the contractile element, the series passive element, and the parallel passive element. In general, the series element describes the tendon force, the parallel element lumps the connective tissue in the muscle and the contractile element lumps the active properties of all sarcomeres in the muscle. An abundance of formulations and different parameterizations can be found in literature, but the general behavior remains the same. In the current implementation, each sarcomere is described by a Hill model with identical properties (although the framework allows setting custom properties per sarcomere).

The sarcomere longitudinal nominal tensile stress $\sigma_{\text{sarc},i}$ is given by,

$$\sigma_{\text{sarc},i} = \underbrace{\sigma_{\text{max},i}\ f_{\text{a},i}(t) f_{\ell,i}(\ell_i) f_{\text{v},i}(\dot{\varepsilon}_i^*)}_{\text{Active } \sim F_{\text{CE}}} + \underbrace{\sigma_{\text{pas,i}}(\varepsilon_i)}_{\text{Passive } \sim F_{\text{PE}}} \tag{B.9}$$

where the subscript i denotes sarcomere i, $\sigma_{\text{max},i}$ is the maximum isometric stress at the sarcomere optimum length, $f_{\text{a},i}$ the activation function, $f_{\ell,i}$ the filamentary overlap function, $f_{\text{v},i}$ the velocity dependence function and $\sigma_{\text{pas,i}}$ the passive stress-strain function. The outputs of the activation function, the filament overlap function and the velocity function are scaled with the maximum isometric stress to obtain the active sarcomere stress for a given sarcomere state.

Starting with the active part in equation (B.9), the sequential activation of the sarcomeres is modelled by the linear increasing activation function $f_{\text{a},i}$. Although we used twitch contractions in the experiment, the model simulates tetanic contractions, avoiding relaxation effects. The Hill model typically needs an input signal in the interval $[0, 1]$, where 0 means no activation and 1 fully activated. The activation function of sarcomere i is given by,

$$f_{\text{a},i}(t) = \begin{cases} 0 & t \le t_{\text{d},i}, \\ \dfrac{t - t_{\text{d},i}}{t_{\text{a},i}} & t_{\text{d},i} < t \le t_{\text{d},i} + t_{\text{a},i}, \\ 1 & t > t_{\text{d},i} + t_{\text{a},i}, \end{cases} \tag{B.10}$$

with $t_{\text{d},i}$ the delay for activation onset and $t_{\text{a},i}$ the time required to reach full activation. The delay for activation onset $t_{\text{d},i}$ for sarcomere i due to propagation time for the action potential along the fiber is given by,

$$t_{\text{d},i} = \frac{\sum_{k=1}^{i-1}(\ell_{\text{optim,k}}) + \frac{1}{2}\ell_{\text{optim,i}}}{V_{\text{ap}}} + t_{\text{ss}} \tag{B.11}$$

with $\ell_{\text{optim},i}$ the optimum length of the sarcomere and t_{ss} a general delay term, and V_{ap} the velocity of the action potential.

The velocity dependence function is based on the formulation by Otten (1987) and is given by,

$$f_{\mathrm{v},i}(\dot{\varepsilon}_i^*) = \begin{cases} \dfrac{1+\dot{\varepsilon}_i^*}{1-\dot{\varepsilon}_i^*/k} & \dot{\varepsilon}_i^* \leq 0, \\ 1.8 - 0.8\dfrac{1-\dot{\varepsilon}_i^*}{1-7.56\dot{\varepsilon}_i^*/k} & \dot{\varepsilon}_i^* > 0, \end{cases} \tag{B.12}$$

where $\dot{\varepsilon}_i^*$ is the normalized strain rate defined as,

$$\dot{\varepsilon}_i^* = \dot{\varepsilon}_i / \dot{\varepsilon}_{\mathrm{max},i}. \tag{B.13}$$

A positive strain rate corresponds to eccentric contraction (lengthening), and a negative strain rate to concentric contraction (shortening).

The filamentary overlap function gives the relation between sarcomere tension and sarcomere length, in literature this is often referred to as the force-length relation. The filamentary overlap function is adapted from van Leeuwen (1991) and is given by,

$$f_{\ell,i}(\ell_i) = \begin{cases} \ell_{\mathrm{myo},i} + \ell_{\mathrm{act},i} + \ell_{\mathrm{z},i} - \ell_i / \ell_{\mathrm{myo},i} - \ell_{\mathrm{bz},i}, & \ell_{\mathrm{act},i} + \ell_{\mathrm{bz},i} + \ell_{\mathrm{z},i} < \ell_i \leq \ell_{\mathrm{myo},i} + \ell_{\mathrm{act},i} + \ell_{\mathrm{z},i}, \\ 1, & \ell_{\mathrm{act},i} + \ell_{\mathrm{z},i} < \ell_i \leq \ell_{\mathrm{act},i} + \ell_{\mathrm{bz},i} + \ell_{\mathrm{z},i}, \\ (\ell_{\mathrm{myo},i} - \ell_{\mathrm{bz},i} - D_{\mathrm{act},i}(\ell_{\mathrm{act},i} + \ell_{\mathrm{z},i} - \ell_i))/(\ell_{\mathrm{myo},i} - \ell_{\mathrm{bz},i}), & \ell_{\mathrm{myo},i} + \ell_{\mathrm{z},i} < \ell_i \leq \ell_{\mathrm{act},i} + \ell_{\mathrm{z},i}, \\ \dfrac{\ell_{\mathrm{myo},i} - \ell_{\mathrm{bz},i} - D_{\mathrm{act},i}(\ell_{\mathrm{act},i} + \ell_{\mathrm{z},i} - \ell_i) - D_{\mathrm{myo},i}(\ell_{\mathrm{myo},i} + \ell_{\mathrm{z},i} - \ell_i)}{\ell_{\mathrm{myo},i} - \ell_{\mathrm{bz},i}} - & \\ \qquad \dfrac{C_{\mathrm{myo},i}(\ell_{\mathrm{myo},i} + \ell_{\mathrm{z},i} - \ell_i)}{\ell_{\mathrm{myo},i} - \ell_{\mathrm{bz},i}}, & \ell_{\mathrm{min},i} < \ell_i \leq \ell_{\mathrm{myo},i} + \ell_{\mathrm{z},i}, \\ 0, & \text{otherwise.} \end{cases} \tag{B.14}$$

When the sarcomere is near to its optimum length, the actin and myosin filaments are overlapping freely, and can form the maximum number of cross-bridges upon activation (Gordon *et al.* 1966). The optimum length of the sarcomere is given by,

$$\ell_{\mathrm{optim},i} = \ell_{\mathrm{act},i} + \ell_{\mathrm{z},i} + \tfrac{1}{2}\ell_{\mathrm{bz},i}. \tag{B.15}$$

When the sarcomere is stretched, the overlap between the actin and myosin filaments decreases. Consequently less cross-bridges can be formed, and the active contraction force decreases. A similar effect happens when the sarcomere is shortened, as the actin filaments then start to overlap, and therefore can form less cross-bridges with the myosin. Parameter $D_{\mathrm{act},i}$ accounts for losses due to actin overlap. Similarly, $C_{\mathrm{myo},i}$ and $D_{\mathrm{myo},i}$ account for losses due to myosin collision and interaction with Z-disks (Van Leeuwen and Kier, 1997).

The passive component in equation (B.9) is adapted from Van Leeuwen and Kier (1997), and given by,

$$\sigma_{\mathrm{pas,i}}(\varepsilon_i) = \begin{cases} 0, & \varepsilon_i \leq 0, \\ c_{\mathrm{pas1},i}\varepsilon_i^{c_{\mathrm{pas2},i}}, & 0 < \varepsilon_i < \varepsilon_{\mathrm{c}}, \\ c_{\mathrm{pas3},i}\varepsilon_i + c_{\mathrm{pas4},i}, & \varepsilon_i \geq \varepsilon_{\mathrm{c}}, \end{cases} \tag{B.16}$$

where ε_c is the critical strain, and $c_{\mathrm{pas1},i}, \ldots, c_{\mathrm{pas4},i}$ are constants.

In the Hill model, typically only elastic passive properties are modelled in the parallel element, although the connective tissue in the muscle is known to have viscoelastic properties (Gennisson *et al.* 2010; Gordon *et al.* 1966; Taylor *et al.* 1990). Therefore, a linear damper is added in parallel to the Hill model, with the damping force in sarcomere i given by,

$$F_{\mathrm{ds,i}} = -c_{\mathrm{damp\text{-}s},i}\ \dot{\ell}_i, \tag{B.17}$$

with $c_{\mathrm{damp\text{-}s},i}$ the damping coefficient for sarcomere i. Furthermore, the additional damping helped the numerical integration of the equations of motion by reducing oscillations in the system.

Finally, the total force in the sarcomere for a given sarcomere state can be determined by,

$$F_{\mathrm{sarc},i} = A_{0,i}\sigma_{\mathrm{sarc},i} + F_{\mathrm{ds,i}}, \tag{B.18}$$

with $A_{0,i}$ the cross sectional area of the sarcomere at optimum length for sarcomere radius $r_{0,i}$,

$$A_{0,i} = \pi r_{0,i}^2. \tag{B.19}$$

Initial sarcomere strain ε_0 was set to 7.5%. This causes some pre-tension of the passive tissue in the muscle, corresponding to the condition in the experiment, though to a lesser extend.

D. Tendon modelling

The tendon is typically modelled by the series elastic element in the Hill model, with only elastic properties. However, like the series elastic element, tendons behave viscoelastic, a property that is often overlooked (Seynnes *et al.* 2014). The tendon is modelled as a linear spring-damper,

$$F_{\text{t}} = (x_n - x_t - \ell_{\text{t0}})k_{\text{t}} + \dot{x}_n c_{\text{t}}, \tag{B.20}$$

where x_n is the position of the last sarcomere boundary, x_t is the position of the distal end of the tendon which remains fixed during contraction, ℓ_{t0} the initial length of the tendon, k_{t} the stiffness of the tendon and c_{t} the tendon viscosity. The stiffness of the tendon is chosen to allow a chosen total fiber strain of $\varepsilon_{\text{fiber,max}}$ at maximum isometric sarcomere stress, i.e.,

$$k_{\text{t}} = \frac{F_{\text{max}}}{\varepsilon_{\text{fiber,max}} \sum_{k=1}^{n} \ell_{\text{optim},k}}, \tag{B.21}$$

where F_{max} is given by,

$$F_{\text{max}} = \max_i(\sigma_{\text{max},i} A_{0,i}). \tag{B.22}$$

The maximum total fiber strain $\varepsilon_{\text{fiber,max}}$ was chosen to be 25%, thus resulting in an initial last fiber boundary position of $x_{m0} = 500\ \varepsilon_{\text{fiber,max}}\ \ell_{\text{optim}}$. If this initial fiber strain is positive, there will be some pre-tension caused by the passive component in the Hill model, given in equation (B.16). The tendon attachment location was chosen such that the elastic force in the tendon was equal to the pre-tension in the fiber. This way, there was no motion in the fiber prior to activation. The initial force in the fiber is given by,

$$F_{\text{sarc0}} = A_{0,i}\sigma_{\text{pas}}(\varepsilon_{\text{fiber,max}}), \tag{B.23}$$

and this force is used to determine the initial elongation of the tendon to make sure that the fiber is in equilibrium. The length change in the tendon to reach the same pre-tension is given by,

$$\Delta\ell_{\text{t0}} = \frac{F_{\text{sarc0}}}{k_{\text{t}}}. \tag{B.24}$$

Finally, the initial position of the last boundary of the system, x_{t}, is given by,

$$x_{\text{t}} = x_m + \ell_{\text{t0}} + \Delta\ell_{\text{t0}}. \tag{B.25}$$

E. Equations of motion

To derive the equations of motion, the m sarcomere boundary positions and tendon end position were chosen as generalized coordinates $\boldsymbol{q}$,

$$\boldsymbol{q} = \begin{pmatrix} x_1 & x_2 & \dots & x_{m-1} & x_m & x_{\text{t}} \end{pmatrix}^T, \tag{B.26}$$

with its time derivatives given by,

$$\dot{\boldsymbol{q}} = \begin{pmatrix} \dot{x}_1 & \dot{x}_2 & \dots & \dot{x}_{m-1} & \dot{x}_m & \dot{x}_{\text{t}} \end{pmatrix}^T, \tag{B.27}$$

$$\ddot{\boldsymbol{q}} = \begin{pmatrix} \ddot{x}_1 & \ddot{x}_2 & \dots & \ddot{x}_{m-1} & \ddot{x}_m & \ddot{x}_{\text{t}} \end{pmatrix}^T. \tag{B.28}$$

The constrained equations of motion (Newton's second law) can be written in the form of a differential-algebraic system of equations (DAE),

$$\begin{pmatrix} \mathbf{M} & \mathbf{C}_{,\boldsymbol{q}}^T \\ \mathbf{C}_{,\boldsymbol{q}} & \mathbf{0} \end{pmatrix} \begin{pmatrix} \ddot{\boldsymbol{q}} \\ \boldsymbol{\lambda} \end{pmatrix} = \begin{pmatrix} \boldsymbol{F}_{\text{ext}} \\ -\mathbf{C}_{,\boldsymbol{qq}}\dot{\boldsymbol{q}}\dot{\boldsymbol{q}} \end{pmatrix}, \tag{B.29}$$

where $\mathbf{M}$ is the diagonal mass matrix, $\mathbf{C}$ the constraint vector, $\mathbf{0}$ a zero matrix, $\boldsymbol{\lambda}$ lagrange multipliers for the constraints and $\boldsymbol{F}_{\text{ext}}$ the external forces applied on the generalized coordinates.

The mass matrix contains the mass of the sarcomeres and tendon. The mass of sarcomere $m_{\text{s},i}$ is distributed equally over the adjacent boundaries. Hence, the mass of boundary x_j is given by,

$$m_j = m_{\text{s},i} + m_{\text{s},i+1}, \tag{B.30}$$

where $m_{\mathrm{s},i}$ and $m_{\mathrm{s},i+1}$ denote the mass of the sarcomere on the left and right of boundary x_j, respectively. The same is done for the tendon mass m_{t}. The mass matrix then becomes,

$$\mathbf{M} = \mathrm{diag}\begin{pmatrix} \frac{1}{2}m_{\mathrm{s},1} \\ \vdots \\ \frac{1}{2}(m_{\mathrm{s},i} + m_{\mathrm{s},i+1}) \\ \vdots \\ \frac{1}{2}(m_{\mathrm{s},n} + m_t) \\ \frac{1}{2}m_t \end{pmatrix}. \tag{B.31}$$

The constraint matrix $\mathbf{C}$ keeps the first and last generalized coordinates fixed, i.e. the position of the left boundary of the first sarcomere and the tendon attachment location respectively,

$$\mathbf{C} = \begin{pmatrix} x_1 \\ x_{\mathrm{t}} - x_{\mathrm{t0}} \end{pmatrix} \tag{B.32}$$

where x_{t0} denotes the initial position of the tendon attachment location. The Jacobian of the constraint matrix is given by,

$$\mathbf{C}_{,\boldsymbol{q}} = \frac{\partial \mathbf{C}}{\partial \boldsymbol{q}}, \tag{B.33}$$

and the convective acceleration terms are defined as,

$$\mathbf{C}_{,\boldsymbol{qq}}\dot{\boldsymbol{q}}\dot{\boldsymbol{q}} = \frac{\partial}{\partial \boldsymbol{q}}\left(\frac{\partial \mathbf{C}}{\partial \boldsymbol{q}}\dot{\boldsymbol{q}}\right)\dot{\boldsymbol{q}}. \tag{B.34}$$

Since the constraints are only dependent on the generalized coordinates and the initial state of the fiber and tendon, these are equal to the zero vector. The lagrange multipliers $\boldsymbol{\lambda}$ associated with the constraints correspond to the reaction forces at the attachment points. The vector with external forces on the boundaries is given by,

$$\boldsymbol{F}_{\text{ext}} = \boldsymbol{F}_{\text{elems}} + \boldsymbol{F}_{\text{damp-q}}, \tag{B.35}$$

where $\boldsymbol{F}_{\text{elems}}$ is a vector that contains the forces of the sarcomeres and tendon, and $\boldsymbol{F}_{\text{damp-q}}$ an additional damping force on the generalized coordinates. The sarcomere and tendon forces can be put in a vector as follows,

$$\boldsymbol{F}_{\text{elems}} = \begin{pmatrix} F_{\text{sarc},1} \\ F_{\text{sarc},2} - F_{\text{sarc},1} \\ \vdots \\ F_{\text{sarc},i} - F_{\text{sarc},i-1} \\ \vdots \\ F_{\text{sarc},n} - F_{\text{sarc},n-1} \\ F_{\mathrm{t}} - F_{\text{sarc},n} \\ -F_{\mathrm{t}} \end{pmatrix}. \tag{B.36}$$

The damping force on generalized coordinate q_j is given by,

$$F_{\text{damp-q},j} = -c_{\text{damp-q},j}\ \dot{q}_j, \tag{B.37}$$

with $c_{\text{damp-q},j}$ the damping coefficient for generalized coordinate j. Since the distal boundaries (close to the tendon) are expected move faster than the proximal boundaries, the damping coefficient is scaled by the initial position of boundary q_j,

$$c_{\text{damp-q},j} = \begin{cases} c_{\text{damp-q}}, & j = 0, \\ \dfrac{c_{\text{damp-q}}}{q_{0,j}}, & j > 0. \end{cases} \tag{B.38}$$

This scaling of the damping can be justified by considering that during a whole muscle contraction the intramuscular fluid will move together with the rest of the muscle structure. Hence the fluid will have a lower relative velocity with respect to the Z-disks then in the modelled fiber, where the surroundings are fixed.

F. Continuous function fits

To further ease the numerical integration, continuous functions were fit to the piecewise continuous force velocity function, filamentary overlap function and passive tension function.

For the filamentary overlap function, an asymmetric Gaussian function was chosen, as demonstrated before by Mohammed and Hou (2016). The continuous filamentary overlap function is given by,

$$f_{\ell\text{-c},i}(\ell_i) = -c_0 + c_1 \exp\left(-\left(\frac{\ell_i - c_2}{c_3 + c_4\ell_i}\right)^2\right). \tag{B.39}$$

The coefficients $c_0, \ldots, c_4$ were optimized by using the curve fitting toolbox of Matlab 2018b. For the other functions, i.e. the force-velocity relation and the passive length-tension relation, an optimal model was chosen using the curve fitting toolbox. For the force-velocity relation, a rational model was chosen, given by,

$$f_{\text{v-c},i}(\dot{\varepsilon}_i) = \frac{p_1\dot{\varepsilon}^5 + p_2\dot{\varepsilon}^4 + p_3\dot{\varepsilon}^3 + p_4\dot{\varepsilon}^2 + p_5\dot{\varepsilon} + p_6}{\dot{\varepsilon}^4 + q_1\dot{\varepsilon}^3 + q_2\dot{\varepsilon}^2 + q_3\dot{\varepsilon} + q_4}. \tag{B.40}$$

For the passive component, a polynomial model wat chosen, given by,

$$\sigma_{\text{pas-c},i}(\varepsilon_i) = g_1\varepsilon^6 + g_2\varepsilon^5 + g_3\varepsilon^4 + g_4\varepsilon^3 + g_5\varepsilon^2 + g_6\varepsilon + g_7. \tag{B.41}$$

Table B1: Fiber model parameters. * denotes a dependent variable.

Symbol	Description	Value	Unit
General parameters			
$\ell_{s0,i}$	initial length sarcomere i	2.295	µm
$\varepsilon_{0,i}$	initial strain sarcomere i	7.5	%
$r_{0,i}$	initial radius sarcomere i	15.0	µm
$A_{0,i}$	initial cross sectional area sarcomere i	706.9	μm^2
$m_{s,i}$	mass sarcomere i	1.5846	ng
ρ	density muscle tissue	1050	$kg\,m^{-3}$
$\sigma_{max,i}$	maximum active stress sarcomere i	100	kPa
Active force-length characteristics			
$\ell_{act,i}$	length of actin filament	2.00	µm
$\ell_{myo,i}$	length of myosin filament	1.60	µm
$\ell_{bz,i}$	length of bare zone myosin filament	0.15	µm
$\ell_{z,i}$	width of Z-disk	0.06	µm
$\ell_{optim,i}$	optimum length sarcomere	* (2.135)	µm
$C_{act,i}$	resistive constant actin filament	0	-
$C_{myo,i}$	resistive constant myosin filament	0.44	-
$D_{act,i}$	constant to account for cross-bridge losses due to actin overlap	0.68	-
$D_{myo,i}$	constant to account for cross-bridge losses due to interaction myosin and Z-disks	1.90	-
Active force-velocity characteristics			
k	constant	0.17	-
$\dot{\varepsilon}_{max,i}$	maximum strain rate	3.5	ms^{-1}
$c_{s,i}$	damping sarcomere i	0	$N\,s\,m^{-1}$
Passive force-length characteristics			
$c_{pas1,i}$	constant in equation B.16	887.4	kPa
$c_{pas2,i}$	constant in equation B.16	2.26	-
$c_{pas3,i}$	constant in equation B.16	1450	kPa
$c_{pas4,i}$	constant in equation B.16	−625	kPa
ε_c	critical strain	0.773	-
Activation characteristics			
V_{ap}	velocity action potential	3.00	$m\,s^{-1}$
$t_{a,i}$	time till full activation sarcomere i	1.00	ms
t_{ss}	general delay activation onset	−0.01	ms
s_n	starting sarcomere number	1	-
Tendon characteristics			
c_t	damping tendon	0	$N\,s\,m^{-1}$
k_t	stiffness tendon	*	$N\,m^{-1}$
ℓ_{t0}	initial length tendon	*	µm
m_t	mass tendon	*	kg

References Fiber Model

Fung, Y. C (2011). *Biomechanics: Mechanical Properties of Living Tissues*. New York: Springer.

Gennisson, Jean-Luc, Thomas Deffieux, Emilie Macé, Gabriel Montaldo, Mathias Fink, and Mickaël Tanter (2010). "Viscoelastic and Anisotropic Mechanical Properties of in Vivo Muscle Tissue Assessed by Supersonic Shear Imaging". In: *Ultrasound in Medicine & Biology* 36.5, pp. 789–801.

Gordon, A. M., A. F. Huxley, and F. J. Julian (1966). "The Variation in Isometric Tension with Sarcomere Length in Vertebrate Muscle Fibres". In: *The Journal of Physiology* 184.1, pp. 170–192.

Hill, Archibald Vivian (1953). "The Mechanics of Active Muscle". In: *Proceedings of the Royal Society of London. Series B-Biological Sciences* 141.902, pp. 104–117.

Huijing, Peter A (1999). "Muscle as a Collagen Fiber Reinforced Composite: A Review of Force Transmission in Muscle and Whole Limb". In: *Journal of Biomechanics* 32.4, pp. 329–345.

Mohammed, G. A. and M. Hou (2016). "Optimization of Active Muscle Force–Length Models Using Least Squares Curve Fitting". In: *IEEE Transactions on Biomedical Engineering* 63.3, pp. 630–635.

Otten, E. (1987). "A Myocybernetic Model of the Jaw System of the Rat". In: *Journal of Neuroscience Methods* 21.2, pp. 287–302.

Seynnes, O. R., J. Bojsen-Møller, K. Albracht, A Arndt, N. J. Cronin, T. Finni, and S. P. Magnusson (2014). "Ultrasound-Based Testing of Tendon Mechanical Properties: A Critical Evaluation". In: *Journal of Applied Physiology* 118.2, pp. 133–141.

Taylor, Dean C., James D. Dalton, Anthony V. Seaber, and William E. Garrett (1990). "Viscoelastic Properties of Muscle-Tendon Units: The Biomechanical Effects of Stretching". In: *The American Journal of Sports Medicine* 18.3, pp. 300–309.

van Leeuwen, J. L. (1991). "Optimum Power Output and Structural Design of Sarcomeres". In: *Journal of Theoretical Biology* 149.2, pp. 229–256.

Van Leeuwen, J. L. and W. M. Kier (1997). "Functional Design of Tentacles in Squid: Linking Sarcomere Ultrastructure to Gross Morphological Dynamics". In: *Philosophical Transactions of the Royal Society of London. Series B: Biological Sciences* 352.1353, pp. 551–571.

Appendix C
EMG signal model parameters

Table C1: Overview of the parameters in the EMG signal model that were fit to the measured EMG signals. The fitting procedure was guided by upper and lower bounds for each parameter. Parameter s was either $\{-1, 1\}$.

Symbol	Description	Lower bound	Upper bound
V_{ap}	Velocity action potential ($\mathrm{m\,s^{-1}}$)	1.5	7
τ_{arr}	Delay due to distance to IZ (ms)	-2	30
A_1	Amplitude of 1st sin (-)	0	10
A_2	Amplitude of 2nd sin (-)	0	10
T_1	Period of 1st sin (ms)	5	70
T_2	Period of 2nd sin (ms)	5	70
θ	Angle of the wave (rad)	-1	1
s	Sign of first sin, either $\{-1, 1\}$	-	-